Postirradiation Examination from Separate Effects Irradiation Testing of Uranium Nitride Kernels and Coated Particles*

Jason M. Harp,† Robert N. Morris, Christian M. Petrie, Joseph R. Burns, Kurt A. Terrani
Oak Ridge National Laboratory, Oak Ridge, Tennessee USA

Abstract

An overview of postirradiation examination results for uranium nitride kernels and uranium nitride coated particles irradiated in the High Flux Isotope Reactor are presented. This is the first postirradiation examination of the MiniFuel irradiation vehicle that was recently developed to rapidly accumulate burnup during separate effects irradiation testing. In general, the burnup and fuel temperatures measured postirradiation were consistent with the design calculations. The burnup measured by mass spectrometry ranged from 5.9 to 10 MWd/kgU and was achieved after only 68 effective full-power days of irradiation. The dilatometric evaluation of passive silicon carbide thermometry indicated that the fuel was irradiated at temperatures ranging from 410 to 460°C. Because the irradiation temperatures and burnup were low, the UN kernels showed minimal fission gas release that was within the range of the expected recoil (athermal) release. While it is possible to measure fuel swelling using x-ray computed tomography, the observed swelling was too small to quantify in this case. Extensive microstructural characterization of the irradiated fuel was performed, and no significant irradiation induced changes were observed.

Keywords: Separate effects; Irradiation testing; Postirradiation examination; Uranium nitride; TRISO

1. INTRODUCTION

Historically, the development and qualification of novel nuclear fuel concepts, and even incremental changes to established nuclear fuel concepts, have been evaluated by iteratively irradiating fuels in prototypic fuel geometries, neutron flux conditions, and temperatures in integral fuel tests that approximated the fuel concept environment. During iterations, conditions were made incrementally more strenuous until fuel failure was observed. This approach was used to establish the acceptable fuel performance envelope for the fuel concept, and it was successful for several fuel concepts that were evaluated in the first few decades of the nuclear industry, with the UO_2–Zircaloy system used in light water reactors being a prominent example. However, this approach is inherently slow and expensive, partly due to the long times needed to irradiate fuel to higher fission densities (i.e., burnup) and perform postirradiation examinations (PIE) on the resulting experiments. It only assesses the fuel system against a narrow set of operating conditions for a specific application, limiting its extension into other slightly different applications. Finally, although the integral tests capture the full effects of prototypic irradiations, they make the elucidation of governing phenomena difficult as they are all superimposed on one another. This process is well documented by Crawford et al. [1] and is expected to require decades to complete.

Renewed interest in novel fuel concepts now demands a more agile approach to irradiation testing. The evaluation of new or minimally studied fuel concepts requires accelerated separate effects testing to rapidly screen fuel concepts at several different irradiation conditions while leveraging modeling and simulation capabilities to target the experimental evaluations of key fuel properties that have the greatest

†Corresponding author. E-mail:harpjm@ornl.gov

impact on fuel performance [2]. The MiniFuel irradiation vehicle is designed to rapidly evaluate nuclear fuel under well-controlled conditions while minimizing the number of variables that occur during irradiation [3]. In MiniFuel irradiations, heating is decoupled from the fission rate so that concepts can be evaluated under a specific condition—such as temperature, composition, and geometry—while simultaneously varying other conditions. Additionally, by decoupling the heating, it is possible to accumulate fission density rapidly compared with prototypic-condition integral testing. The result is the accelerated screening of concepts in the separate-effects stage of testing. Separate-effects tests, such as those planned for MiniFuel, can be used to collect data and develop parameters for models of different irradiation-induced phenomena, or they can be used to confirm existing mechanistic models. This is particularly important in current modeling efforts because the highly detailed and computationally intensive investigations that focus on first-principle calculations require large amounts of data under many different irradiation conditions to achieve high-fidelity phenomena modeling with the minimum number of empirical parameters. Once well validated, mechanistic models can then be used to predict the behavior of the same fuel concepts in an integral test. This approach to fuel testing increases the efficiency of integral testing at prototypic conditions by screening poor fuel concepts and providing foundational data of fuel performance before integral testing is performed [2].

2. SUMMARY OF IRRADIATION TEST

The design of the MiniFuel irradiation vehicle is documented in Petrie et al. [3] and is illustrated in Figure 1. In this test, small fuel samples are placed in compatible material cups (Mo in the first MiniFuel irradiations) that are then sealed inside a capsule that contains a relatively massive high atomic number filler material (again, Mo in the initial irradiation). The filler material generates most of the heat within the capsule through gamma heating rather than fission heating in the fuel sample itself. The filler also contains a silicon carbide (SiC) temperature monitor (TM) that can be evaluated in PIE to give an indication of the terminal irradiation temperature [4]. The current design includes six capsules inside a single target capsule that is then placed into a basket that locates the experiment in a specific location in the High Flux Isotope Reactor (HFIR) outer reflector. The thickness and composition of the stagnant gas in the gap between the target capsule inner diameter and capsule outer diameter are used to control the conductance, therefore the temperature of the fuel samples; this gas is typically He.

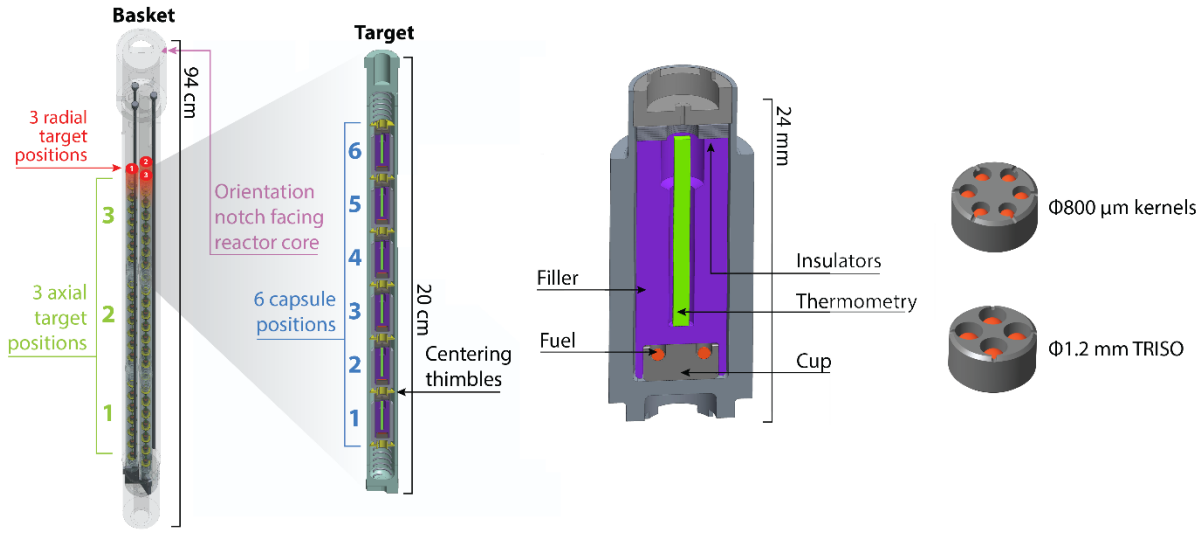

Figure 1. The MiniFuel irradiation test vehicle [3].

The initial fuel evaluated in MiniFuel irradiations is related to the development of uranium nitride (UN) tristructural isotropic (TRISO) fuel [5]. This fuel form was developed as a high actinide density variation on TRISO fuel, building on the long history of this microencapsulated fuel form with the most

recent developmental efforts performed under the US Department of Energy (DOE) Advanced Gas Reactor program [6–11]. This utilization of nitrides in coated particle nuclear fuel is different from historical applications of nitrides for fast reactors as driver fuel [12, 13] or as an actinide destruction targets [14, 15]. This irradiation seeks to further investigate the performance of this fuel form, and specifically, the uranium nitride (UN) kernel, to help inform and optimize fuel fabrication parameters for UN TRISO, such as coating layer thickness and coating parameters, which are based on the best available and yet sparse data and models [16].

To this end, the irradiated MiniFuel targets contained uranium nitride (UN) kernels with four different composition variations and a density variant. What is referred to in this study as *UN* is a solid solution of uranium mononitride and monocarbide U(C,N). At the burnups targets for these irradiations and the target temperatures high carbon impurities are not expected to impact swelling and fuel cladding chemical interaction, that may be exasperated by high carbon contents, is not an issue in this irradiation design or the UN TRISO fuel form [12, 17]. In these tests, kernels with different C/N ratios were examined. Also, kernels with an integral burnable absorber (i.e., Gd addition) were included [17, 18]. Finally, UN TRISO particles in which the various coating layers surround the UN kernel were included. The irradiation matrix is shown in Table 1, and more details about the samples are documented in the literature [19–23].

Table 1. Pre-irradiation properties and target irradiation conditions for the MiniFuel MF01 and MF02 targets.

Capsule ID and position by RAS* (MF01/MF02)	Fuel form	Kernel theoretical density (%)	Density (g/cm^3)	^{235}U enrichment (wt.%)	Burnup target	Target temperature (°C)
221/321	$UC_{0.20}N_{0.80}$ kernels	94.9	13.598	0.22	1% FIMA/ 6% FIMA	500–600
222/322	$UC_{0.15}N_{0.85}$ kernels	90.6	12.981	0.71		
223/323	$U_{0.89}Gd_{0.11}C_{0.11}N_{0.89}$ kernels	92.0	13.178	0.71		
224/324	$U_{0.98}Gd_{0.02}C_{0.15}N_{0.85}$ kernels	93.6	13.41	0.71		
225/325	$UC_{0.21}N_{0.79}$ kernels	90.9	13.02	0.22		
226/326	$UC_{0.20}N_{0.80}$ TRISO particles	87.2	12.49	0.22		

*(R = radial target position, A = axial target position, S = subassembly position)

The conditions of this irradiation for UN is quite unique compared to the historic database which focused on fast breeder reactor applications[17]. Although prior work tested the irradiation performance of sol-gel-derived uranium carbide (UC) kernels [24], this work presents the first measurements of the irradiation performance of sol-gel-derived UN. Previous irradiations of traditionally pressed and sintered UN pellets showed considerable variations in fuel swelling [25] and fission gas release [26]. Fuel swelling and fission gas release are known to depend on temperature, burnup, density, temperature gradient, stoichiometry, impurities, and grain size [12, 13, 26]. Unfortunately, all these parameters are not well documented in historic irradiation tests, resulting in significant uncertainties in predicting fuel performance.

In June 2018, two MiniFuel targets were designated as *MF01* and *MF02* and were inserted into HFIR in the Vertical Experiment Facility (VXF)-15 irradiation position [20]. Figure 2 shows the pre-irradiation photos and x-ray radiography of these targets. The basket used for this irradiation has three radial target

positions, each containing three axial target positions. A target position is specified as *R*-*A*, where *R* is the radial target position, and *A* the axial position in the basket. Radial positions 2 and 3 face toward the core, and radial position 1 is partially shielded from the core by the other positions. This is illustrated on the left side of Figure 1. The MF01 target had a burnup goal of 1% fissions per initial heavy metal atoms (FIMA) and was in the 2-2 position in the MiniFuel basket. The MF02 target has a burnup goal of 6% FIMA and is located at the 3-2 position in the HFIR basket. Within each target, the six capsules were numbered from the bottom to the top of the core by using the integers 1 to 6. The positioning of each capsule also served as its identifying mark for PIE (see Table 1).

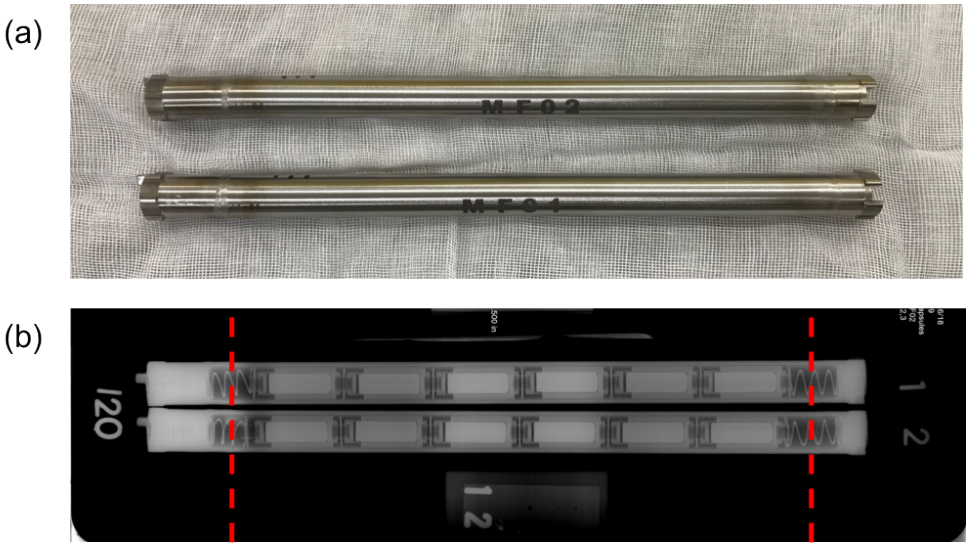

Figure 2. Pre-irradiation (a) photography and (b) x-ray image of the MF01 and MF02 targets; the red dashed lines indicate PIE cuts [28]**.**

The as-fabricated, as-run irradiation conditions experienced by the MiniFuel were simulated by the simulation methodology as described in Petrie et al. [3] and are briefly summarized here. Heat generation rates in the targets were calculated during a HFIR cycle by using a Monte Carlo radiation transport code coupled with a weight window optimizer and a production depletion code. The heat generation rates were then transferred to an ANSYS finite element model of the target to evaluate the fuel specimen temperatures. The MF01 target completed its third cycle on September 28, 2018 (HFIR cycle 482) after approximately 68 effective full-power days of irradiation. This resulted in a fast neutron fluence ($E > 0.1$ MeV) of approximately 3.2×10^{20} n/cm^2 for all the samples in this test. The target was then inserted into HFIR cycle 483, but no burnup was accumulated because this cycle was ended during start-up testing. The target was then discharged for PIE.

3. POSTIRRADIATION EXAMINATION TECHNIQUES

After irradiation, the MF01 target was transferred from HFIR to the ORNL Irradiated Fuel Examination Laboratory (IFEL). The PIE executed to evaluate the initial MiniFuel irradiation performance included retrieving the capsules from the target, measuring the fission gas released to each capsule, removing the fuel and thermometry from the capsule, evaluating the individual samples by gamma spectrometry, and evaluating select particles by x-ray computed tomography (XCT). This was followed by optical and electron microscopy. The burnup of one sample from each of the kernel-containing capsules was also evaluated by mass spectrometry to further benchmark the experiment.

3.1 Target Capsule Disassembly

After the targets were received at the hot-cell, the bottom endcap of the target capsule was cut with a low-speed saw [28], and the capsules from MF01 were removed. These cuts went as planned, and the capsules were easily removed from the target.

3.2 Fission Gas Release Measurements

The fission gas release of all MiniFuel samples was evaluated by measuring the fission gas present in the free gas volume of each capsule. The Kr-85 inventory was measured by passing the capsule fill gas through a liquid-nitrogen–cooled charcoal trap system. The captured Kr-85 was then counted on a high purity germanium (HPGe) detector system calibrated by a special form source that was designed to mimic a trap. The trap system comprised two traps in series, so any breakthrough or leakage through the first trap would be noticed and captured. Both traps were counted after the puncture test, and the first trap was recounted hours or days after the first count to monitor for any short-term leaks that might have occurred. No significant leakage was noted in any of the traps used. Between tests, the traps were heated up to 200–250°C for 90 minutes under vacuum to evacuate the Kr-85 from previous tests. The traps were then recounted to ensure that they were empty before beginning the next test.

The schematic of the puncture system is shown in Figure 3. First, the system is pumped down to check for leaks, the sample bottle (i.e., known reference volume) is used to compute the tare volume of the system, the system is pumped down again, and the MiniFuel capsule is punctured. The released gas pressure is measured as a function of time, as shown in Figure 4. Finally, gas flow is established through the system, which pushes the released gas through the cooled trap system. After approximately 1 hour, the traps are removed and allowed to warm up. Then they are gamma counted the first time and recounted to investigate for reproducibility and/or leaks. The capsule free gas volume was also measured, but the volume was so small that the measurement uncertainty is too large for analysis.

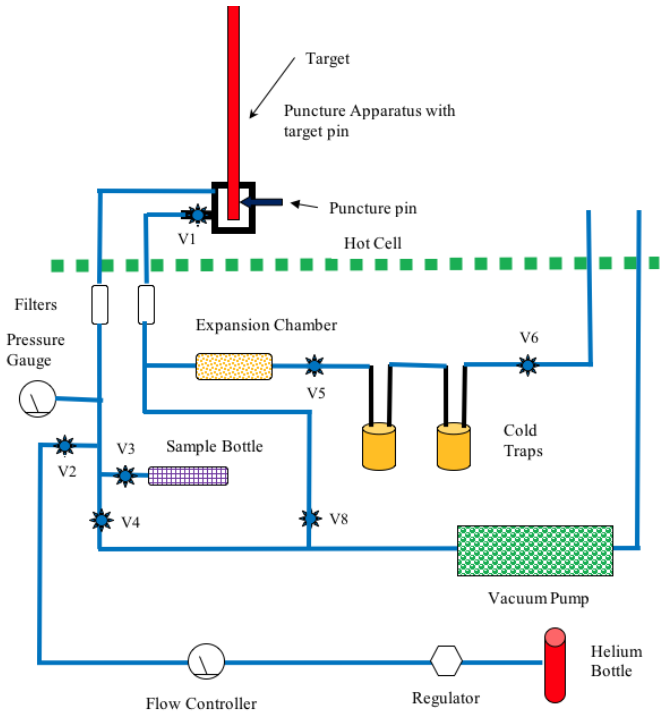

Figure 3. Schematic of the puncture system.

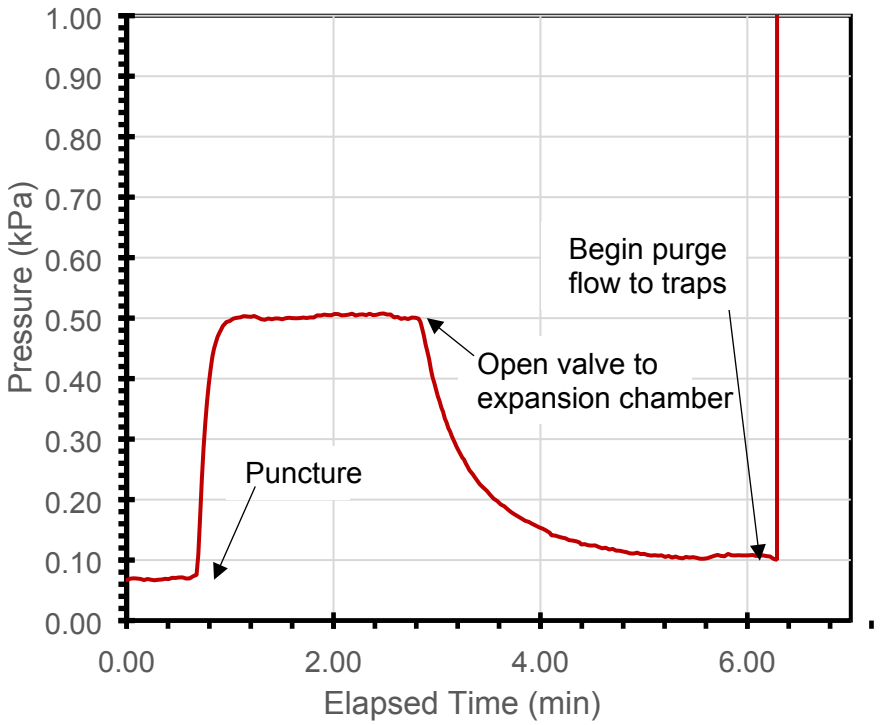

Figure 4. Pressure rise and expansion during the puncture of MiniFuel Capsule 221.

The activities of Kr-85 measured by the gas puncture tests are shown in Table 2. In general, the gas release was small in all capsules. There was considerable uncertainty from counting statistics for some capsules for which the detectable amount of Kr-85 was <1 μCi. No detectable Kr-85 was present in Capsule 226, which was as expected since this capsule contained TRISO particles. The fission gas release fraction for the measured amount of Kr-85 is also given in Table 2. The measured Kr-85 activities are normalized by the calculated Kr-85 source activity in each fuel sample to determine fission gas release. Burnup calculations were verified by mass spectrometry, as shown in Section 3.7.

Table 2. Measured Kr-85 activities and calculated fission gas release for each capsule.

Capsule	Kr-85 activity (μCi)	Fission gas release (%)
221	0.045 ± 0.006	0.16 ± 0.02
222	1.015 ± 0.010	2.09 ± 0.02
223	1.080 ± 0.019	3.49 ± 0.06
224	0.014 ± 0.004	0.03 ± 0.01
225	0.022 ± 0.005	0.08 ± 0.02
226	<0.008	N/A

3.3 Capsule Disassembly and Sample Recovery

After puncturing, the top weld of the capsules was sectioned off using a low-speed saw and a positioning fixture to maintain sample orientation and retain the SiC thermometry. The opened capsules were capped to retain their geometry and transferred from the main hot-cell to an auxiliary hot-cell where operators have superior handling, viewing, and control of small samples. This cell is known as the *irradiated microsphere gamma analysis (IMGA)* cell. The IMGA cell is also equipped with a stereomicroscope and vacuum needle system that allows operators to select and sort individual spherical particles or other small items, such as the SiC TMs. Care was taken to recover the inner dish that contained particles while maintaining the identities of the particles from pre-irradiation loading configuration. However, it was only possible to maintain particle identification on three of the six capsules: Capsules 221, 225, and 226. The stereomicroscope was used to provide visual examination of the MiniFuel specimens. Visual examinations showed that the chemistry variations in the UN kernels tested in this target did not notably affect the fuel behavior at this burnup level. An example of the kernels from Capsule 221 is shown in Figure 5(a). The UN TRISO particle fuel also survived irradiation intact, as shown in Figure 5(b). An example of the recovered SiC thermometry is shown in Figure 6. All 34 particles were recovered from the capsules and placed in individual sample vials for subsequent PIE, starting with gamma counting.

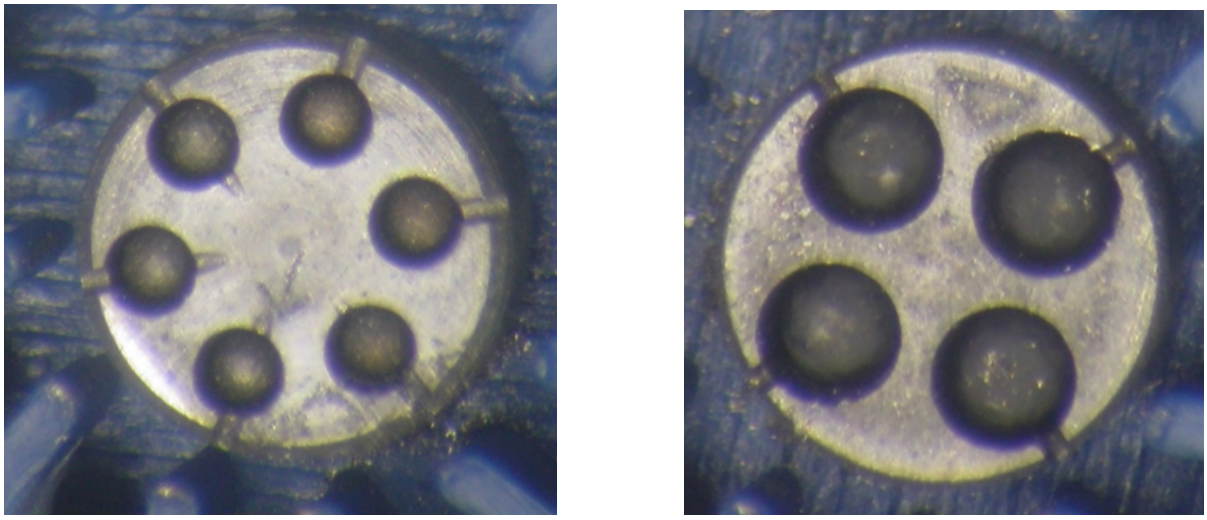

(a) (b)

Figure 5. (a) $UC_{0.20}N_{0.80}$ kernels from MiniFuel Target MF01, Capsule 221; (b) $UC_{0.20}N_{0.80}$ TRISO particles from MiniFuel Target MF01, Capsule 226 (Mo holders are 6 mm in diameter).

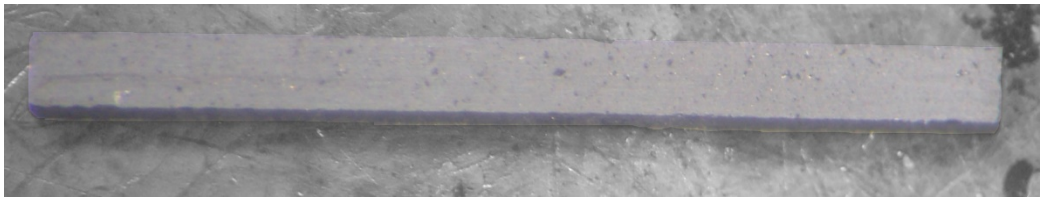

Figure 6. SiC thermometry recovered from MiniFuel Target MF01, Capsule 222 (13 mm long).

3.4 Gamma Counting

The individual fuel particles from each capsule were gamma counted in the IMGA cell using a collimated HPGe detector integrated into that cell. Gamma spectrometry can be used in a variety of ways to characterize the fuel particles and target specific particles for enhanced study. In addition to the particles, any debris from disassembly and the Mo cups that held the particles were gamma counted to determine if there was any significant fission product release from the kernels. For the particles that did not have their identities preserved in disassembly (Capsules 222, 223, and 224), the measured activity of their different radionuclides can be used to map different particles back to the pre-irradiation masses to provide a partial identification. The activity of Cs-137 and the ratio of the activity of Cs-134 to Cs-137 can be used to assess the burnup of the individual fuel particles [29]. These experimentally determined burnup values can provide an initial comparison to burnups calculated from the neutronics simulations. Gamma spectrometry can also provide some information regarding relative contributions to burnup from fission of U-235 vs. Pu-239. For example, Ru-106 has a much higher fission yield from Pu-239 fission than U-235 fission. This causes the Ru-106 to Cs-137 ratio to be higher in the depleted uranium kernels than in the natural uranium kernels.

A limited set of important fission product activities for all 34 particles are included as supplementary data in Table S.1. The activities were decay corrected back to the end of the last HFIR cycle that was at full power (September 28, 2018). The gamma spectrometry results were also used to screen particles for mass spectrometry and optical microscopy to ensure that particles with a representative content of gamma-emitting isotopes were evaluated and particles whose activities were outliers were not evaluated extensively.

3.5 SiC Thermometry

Each MiniFuel capsule contained a 13 × 1 × 1 mm parallelepiped SiC TM. These TMs are evaluated by continuous dilatometry [4] to determine the average temperature of each TM over the last two cycles of irradiation. The average irradiation temperature for all capsules was very similar. The average temperature evaluated by the dilatometry method was 403° ± 5°C. The measured temperature of the SiC can be compared with finite element simulations of the MiniFuel capsules to determine the fuel irradiation temperature [3]. Table 3 provides the temperatures that were determined for each capsule from the passive SiC TMs. The fuel temperatures inferred from these measurements are explained further in the discussion.

Table 3. Temperatures determined for each capsule from the passive SiC TMs.

Capsule	Measured temperature (°C)
221	403
222	403
223	406
224	406
225	402
226	394

3.6 X-Ray Computed Tomography

X-ray computed tomography (XCT) has been used to evaluate a portion of the irradiated MF01 particles. With XCT, the volume of uncoated particles and the kernel volume and layer integrity of coated particles can be measured. At this burnup, any irradiation-induced swelling of the fuel is too slight to allow for measurement of a volume change. At this writing, one UN TRISO particle has been evaluated by XCT, and no large radial defects in any of the coating layers were visible. No pre-irradiation XCT

measurement of the coated particles was performed which makes volume comparisons difficult. The kernel diameter with uncertainty measured from XCT falls within the distribution of the diameters for the source kernels. Two other TRISO particles will be evaluated in future examinations in conjunction with heating tests.

3.7 Mass Spectrometry

The chemical composition of a sample of MiniFuel kernels was evaluated by mass spectrometry, and the resulting data were used to determine the burnup of the fuel in the sampled capsules and compare them with neutronics simulations and gamma spectrometry. A particle from each of the five capsules that contained bare kernels was dissolved for mass spectrometry analysis. The five particles were dissolved in 8N heated nitric acid, and the dissolved samples were then evaluated on a series of mass spectrometers to determine the actinide and fission product content of the fuel. The details of this analysis are not repeated here, but the techniques used to collect this data are recorded in other works [30–34].

3.8 Microscopy

Particles from each capsule were selected for optical microscopy. The selected particles were mounted in epoxy, ground, and polished. Optical microscopy was performed using a Leica Model DMI5000M inverted microscope. Images were collected with an integrated Leica DFC490 digital camera at several different magnifications. Examples from the six MiniFuel capsules are shown in Figure 7 through Figure 12. The same mounts that were prepared for optical microscopy were also examined via scanning electron microscopy (SEM).

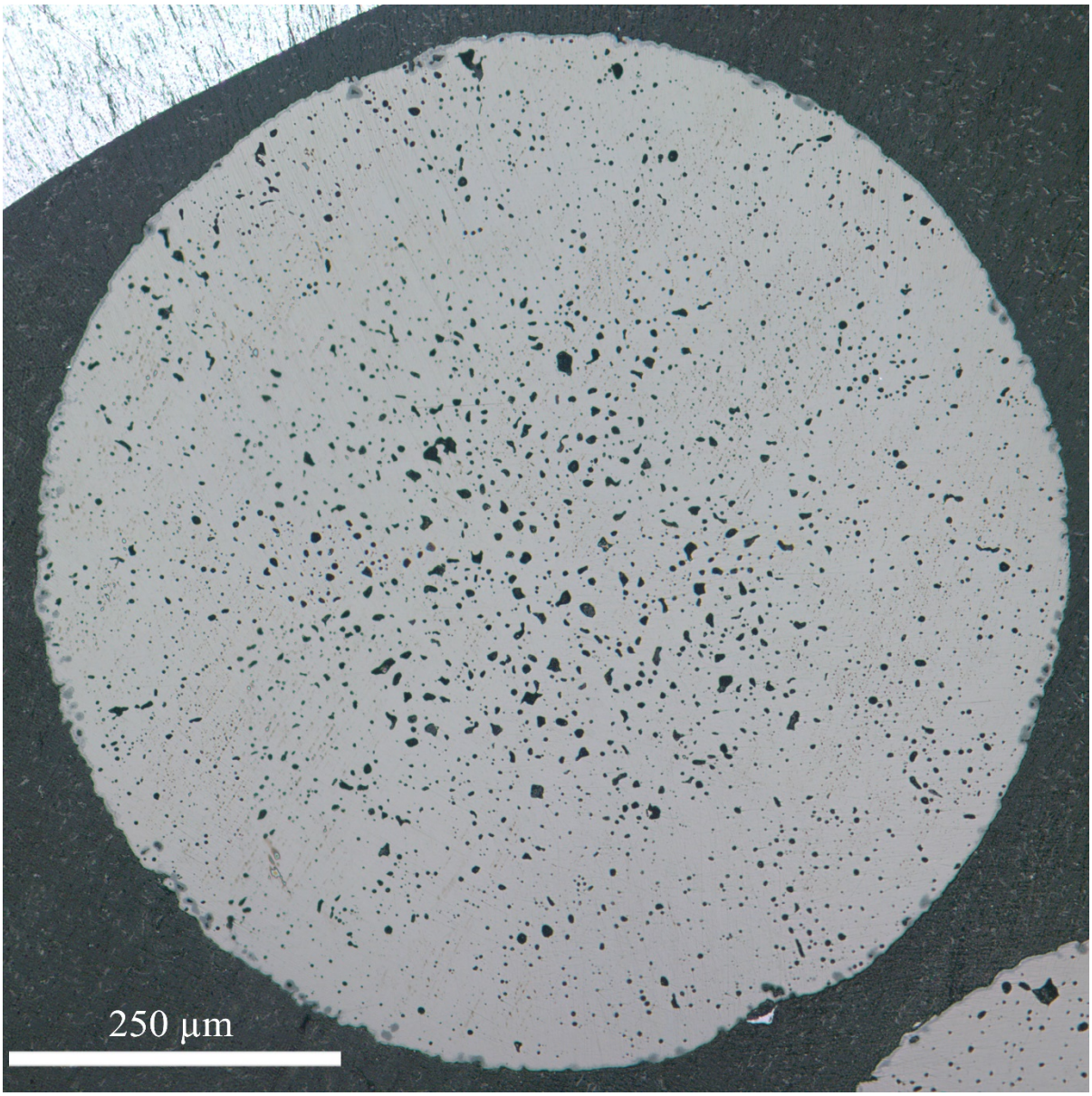

Figure 7. Optical microscopy of $UC_{0.20}N_{0.80}$ particle, MF01 221-02, irradiated to 6.0 MWd/kgU.

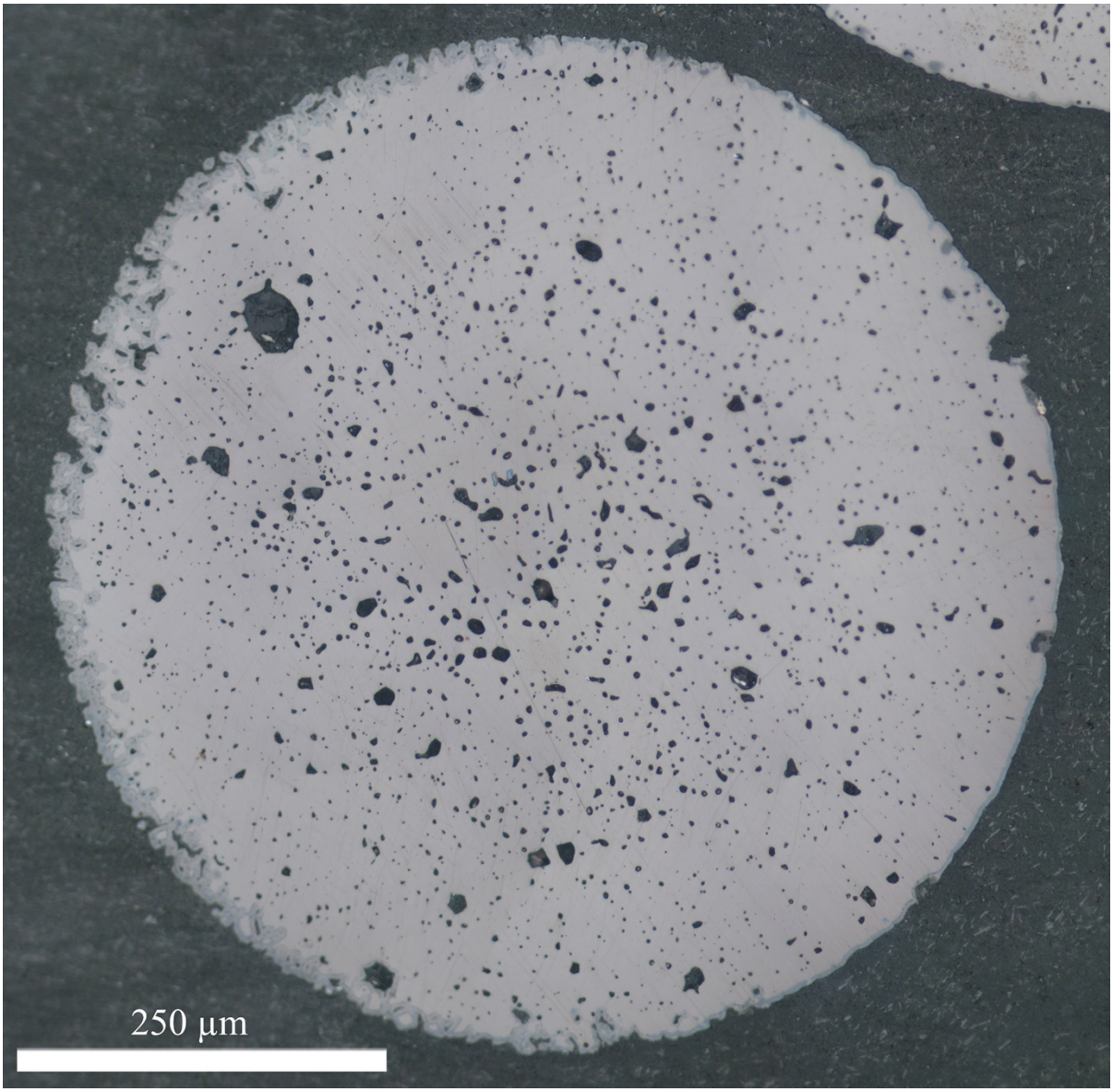

Figure 8. Optical microscopy of $UC_{0.15}N_{0.85}$ particle, MF01 222-02, irradiated to 9.1 MWd/kgU.

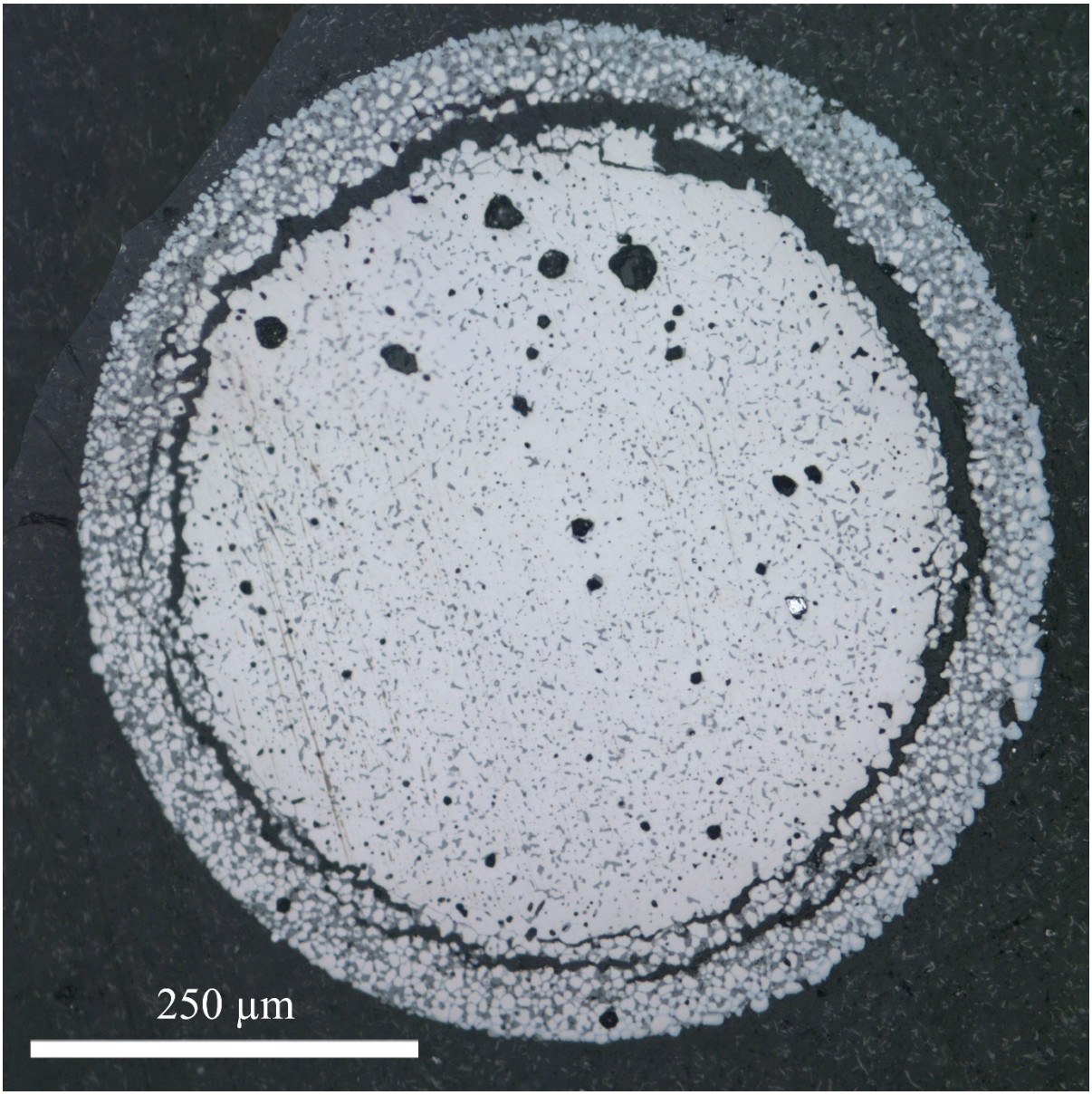

Figure 9. Optical microscopy of $U_{0.89}Gd_{0.11}C_{0.11}N_{0.89}$ particle, MF01 223-04, irradiated to 9.2 MWd/kgU.

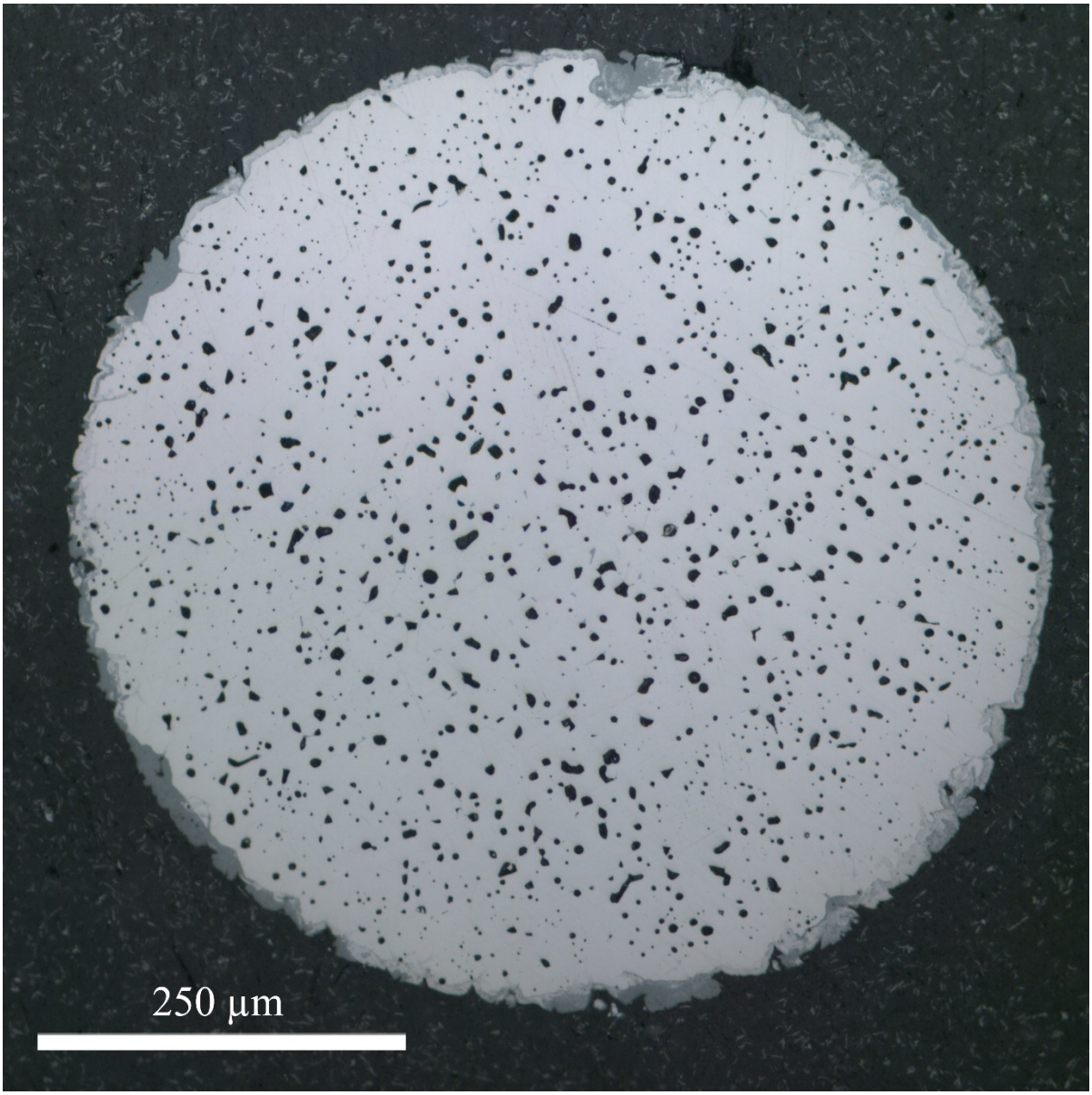

Figure 10. Optical microscopy of $U_{0.98}Gd_{0.02}C_{0.15}N_{0.85}$ particle, MF01 224-02, irradiated to 9.2 MWd/kgU.

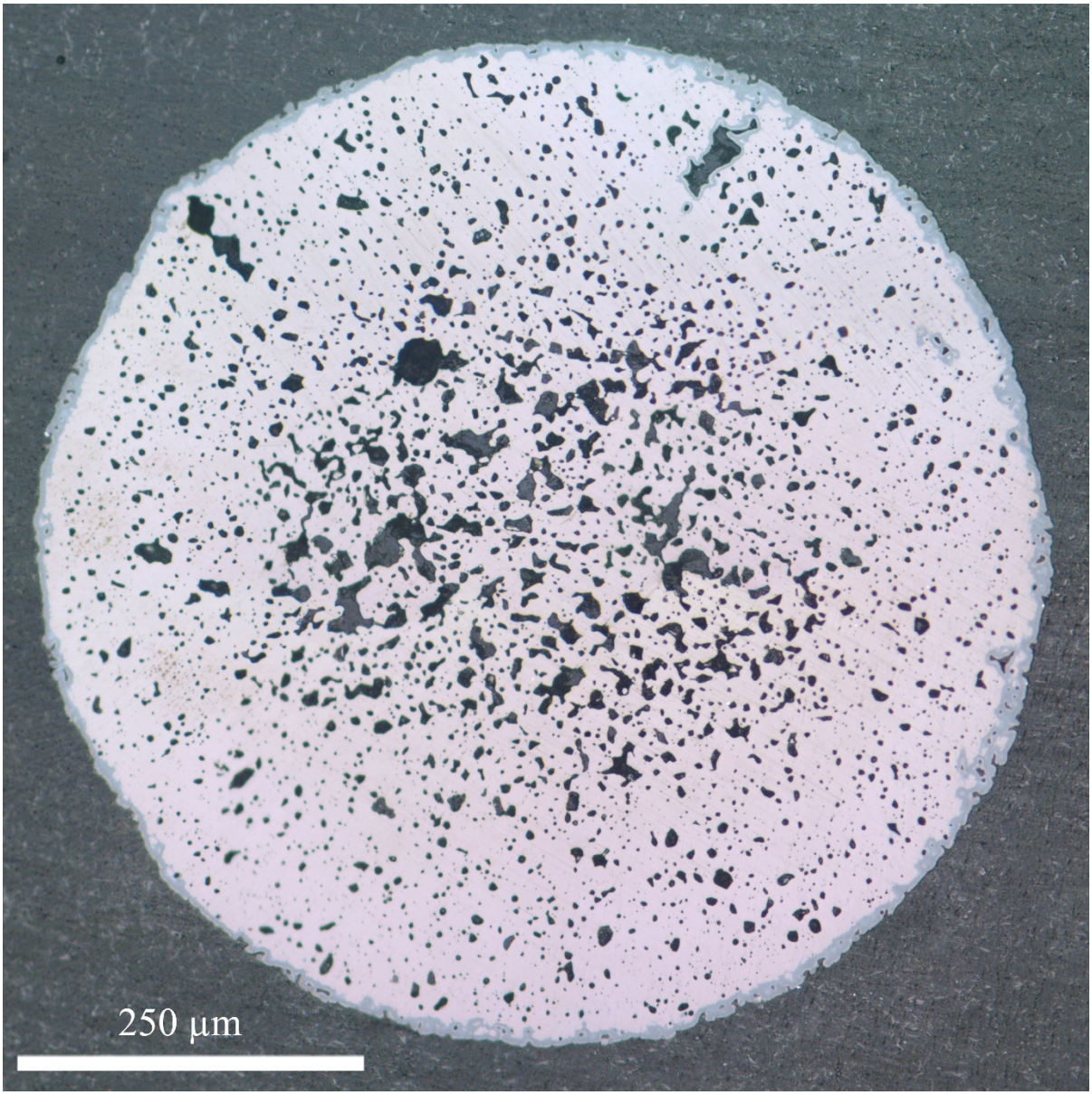

Figure 11. Optical microscopy of $UC_{0.21}N_{0.79}$ particle, MF01 225-06, irradiated 6.2 MWd/kgU.

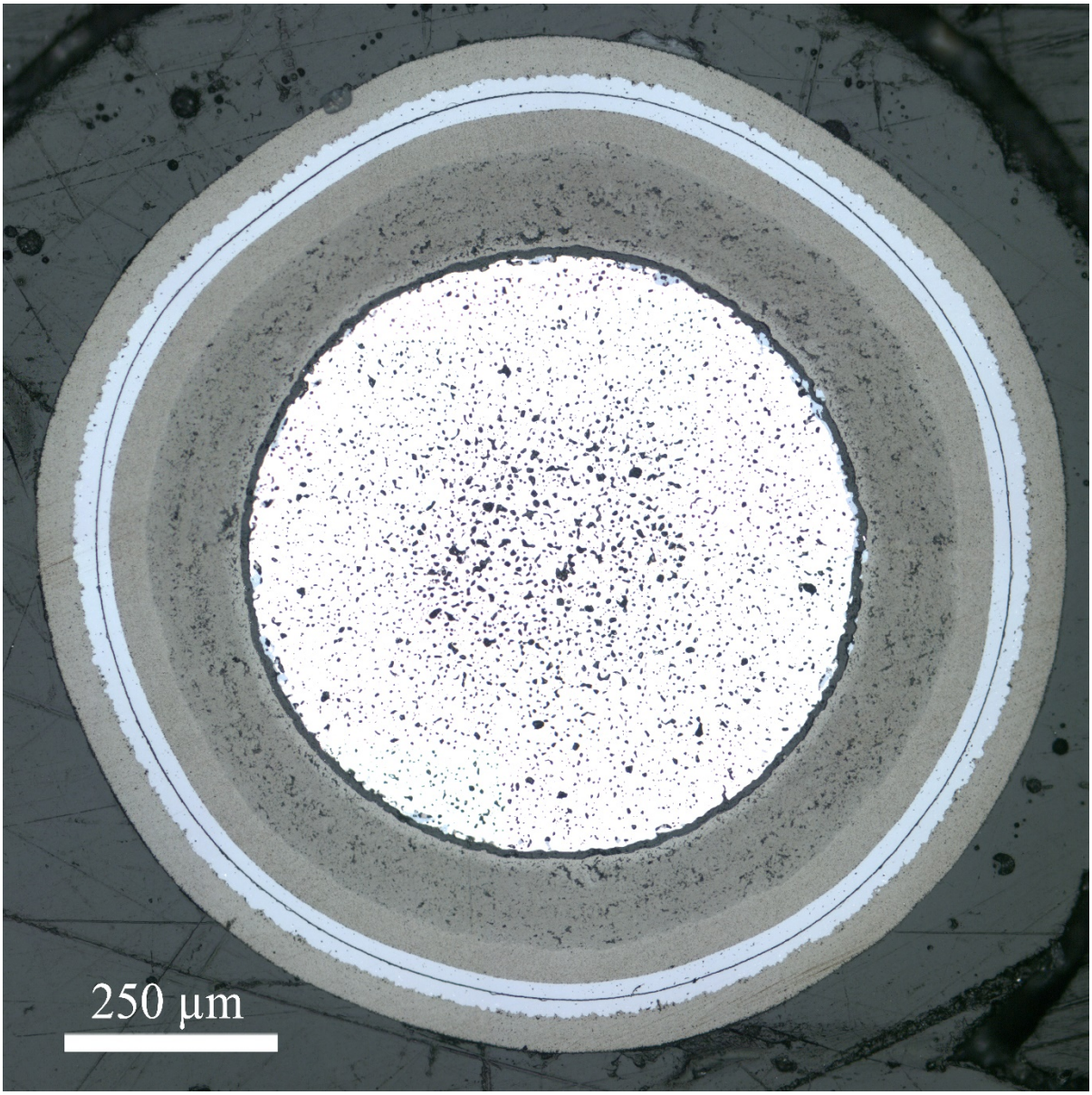

Figure 12. Optical microscopy of $UC_{0.20}N_{0.80}$ TRISO-coated particle, MF01 226-04, irradiated to 6.5 MWd/kgU.

4. RESULTS AND DISCUSSION

MiniFuel PIE was successful, especially for the first PIE of a new irradiation vehicle. A few lessons were learned related to capsule labeling and the need for a more robust method for final capsule disassembly to increase the reliability of maintaining particle identity. This improvement is necessary for pre-irradiation and postirradiation characterization comparisons of factors, such as the volume and mass of the individual samples, which are critical for the high-precision evaluation of swelling.

4.1 Observed Irradiation Conditions Compared with Simulation

For new irradiation vehicles, it is especially important to verify that the methods used to predict and simulate the irradiation conditions are producing results consistent with experimental observations. For fuels irradiations, the ability to accurately predict burnup accumulation and isotopic evolution is critical. Table 4 shows the burnup predicted by the as-run simulations and the measured burnup evaluated by several different methods. The average capsule burnup ascertained by Cs-137 content is determined by a modified "Fission Product Monitor—Residual Heavy Atom" technique [28, 34] in which the number density of actinides was assumed to be constant during the short irradiation. Burnup was also determined from the average capsule Cs-134/Cs-137 activity ratio using the same technique outlined in Harp et al. [29]. The mass spectrometry-based burnup was also determined using the "Fission Product Monitor—Residual Heavy Atom" technique [28, 34] using two sets of nuclides. The following nuclides were used in the "Lanthanide Average" burnup determination: La-139, Ce-140, Pr-141, Ce-142, Nd-145, Nd-146, and Nd-148. The Nd-148 based burnup values were determined from the Nd-148 content solely. A weighted average of the U-235 and Pu-239 thermal neutron fission product yield for each nuclide was used for each capsule based on the relative proportion of each measured nuclide. The Nd-148 -based burnup has the advantage of a roughly equivalent yield for U-235 fission and Pu-239 fission.

Table 4. Predicted and measured burnup of fuel in MiniFuel capsules evaluated by different methods.

		Gamma spectrometry		Mass spectrometry	
Capsule	**Simulation (MWd/kgU)**	**^{137}Cs activity (MWd/kgU)**	**^{134}Cs/^{137}Cs ratio (MWd/kgU)**	**Lanthanide average (MWd/kgU)**	**^{148}Nd (MWd/kgU)**
221	6.0	5.5 ± 0.3	5.7 ± 0.3	5.2 ± 0.3	5.9 ± 0.3
222	9.1	9.3 ± 0.5	8.2 ± 0.4	8.2 ± 0.4	9.1 ± 0.5
223	9.2	6.8 ± 0.3	8.7 ± 0.4	8.6 ± 0.4	9.5 ± 0.5
224	9.2	7.2 ± 0.4	8.4 ± 0.4	8.9 ± 0.4	10 ± 0.5
225	6.2	4.6 ± 0.2	5.8 ± 0.3	5.5 ± 0.3	6.0 ± 0.3
226	6.5	5.9 ± 0.3	6.1 ± 0.3		

The neutronics simulations appear to capture adequately the fission and transmutation process that drives burnup accumulation in the MiniFuel capsules. Feedback from the isotopic results of the MF01 target will be used to improve the simulations used in the design and continued irradiation of the many MiniFuel capsules that are currently being built or are already in the reactor. With the exception of the Cs-137 activity based burnup measurements, these different burnup measurements are in good agreement (within ~15% or less) with the simulations to the limit of experimental accuracy. The greatest disagreement between simulations and measurement techniques occurs for the Cs-137 based burnup for Capsules 223, 224, and 225. However, the mass spectrometry-based measurements for these capsules agree well with simulation.

For MiniFuel experiments, particularly those with lower enrichments or natural uranium, the production and fission of Pu is especially important and eventually dominates burnup accumulation once

an equilibrium between Pu-239 breeding (from U-238) and burning has been reached [3]. As shown in Table 5, the absolute Pu-239 content per particle predicted by simulations does not differ too much from the measurements at this burnup. For all capsules except Capsule 225, the absolute Pu-239 mass per particle predicted by the simulations is within ±15% of the measured Pu-239 mass. The simulations overpredict the Pu-239 mass per particle in Capsule 225 by ~27%. The simulations underpredict the ratio of Pu-239 to U-238, and they underpredict the ratio of Pu-239 to Pu-240. For Pu-239/U-238, the simulations might be underpredicting the conversion of U-238 to Pu-239, or overpredicting the destruction of Pu-239 by fission or neutron capture. The ratio of Pu-239/Pu-240 in the simulation is lower than in the experimental data, which indicates the overprediction of Pu-239 destruction by fission. This discrepancy might not have significantly impacted burnup at current levels, but this difference will be monitored to ensure that future MiniFuel experiments, particularly those that rely on Pu-239 fission to achieve higher burnup, are discharged at the appropriate cycle to meet their burnup targets.

Table 5. Relative Pu isotopics from mass spectrometry compared with simulations.

	Pu-239 mass per particle (μg)		Pu-239/U-238		Pu-239/Pu-240	
Capsule	**Simulation**	**Mass spectrometry**	**Simulation**	**Mass spectrometry**	**Simulation**	**Mass spectrometry**
221	14.0	14.3	3.7E-03	4.2E-03	2.9	3.3
222	12.7	14.1	3.8E-03	4.2E-03	2.9	3.3
223	10.7	9.3	4.0E-03	4.6E-03	2.9	3.3
224	16.7	15.1	3.8E-03	4.5E-03	2.8	3.3
225	17.2	13.5	3.8E-03	4.3E-03	2.8	3.4

The irradiation temperatures determined via the dilatometric analysis of the passive SiC TMs can also be compared with the thermal design calculations. Following the methodology established previously [20], three-dimensional ANSYS finite element simulations were performed by using the nuclear heating rates determined from Monte Carlo N-Particle (MCNP) and ORIGEN. Table 6 compares the postirradiation measured and pre-irradiation calculated temperatures of the TMs in each capsule. Table 6 also includes the pre-irradiation calculated fuel temperatures which are about 100°C higher than the TM's. After compensating for the observed differences in calculated vs. measured TM temperatures, postirradiation compensated temperatures were determined from the TM measurements with the ANSYS simulation. The calculated temperatures shown in Table 6 are for the end of the irradiation. Thus, the temperature of the fuel during irradiation was about 50°C less than designed. This difference is being used to refine the simulation of future MiniFuel irradiations.

Table 6. Comparison of measured vs. calculated average component temperatures.

Capsule	Postirradiation Measured TM temperature (°C)	Pre-Irradiation Calculated TM temperature (°C)	Pre-Irradiation Calculated fuel temperature (°C)	Postirradiation Compensated fuel temperature (°C)
221	403	454	502	451
222	403	453	512	462
223	406	448	513	471
224	406	455	514	465
225	402	455	499	446
226	394	453	504	445

The calculated TM temperatures were approximately 50°C higher than the measured values. Referring to the simulated temperature profiles determined previously [3], most of the temperature variation (~350°C) within the experiment occurs through the ~0.3 mm gas gaps between the capsules and the inner surface of the target. The only other significant temperature variation (~50°C) occurs within the gap between the inner surface of capsule and its contents. The average temperatures of the fillers, cups, and TMs (i.e., the contents of the capsule) are equal to within <5°C. Because the calculated burnup generally agrees with the postirradiation measurements, there is confidence that the fuel heating rates were accurately calculated. This also implies that the calculated difference in temperature between the fuel and the TMs is correct. The discrepancies between the calculated vs. measured TM temperatures are most likely related to the calculation of heat transfer through the filler/capsule and/or the capsule/target gas gaps. The critical inputs to the gap heat transfer calculations are the diameters of the components and the gamma heating rates in the structural materials. The diameters of the capsules used in the model were identical to the as-built dimensions. The modeled target inner diameter was 0.01 mm larger than the as-built value, but this discrepancy would result in the capsule temperatures being at most 6°C cooler than the as-calculated values. The as-built gaps between the filler and capsule were 0.02 to 0.035 mm larger than the modeled values, which would result in the temperature difference through the filler/capsule gap being 7–12°C higher than predicted by the model. The composition of the fill gas used in the experiment was a 41.93% He, Ar balance mixture. This mixture has slightly more He than the 40.5% He, Ar balance mixture used in the design calculations, which would decrease temperatures by ~12°C.

The last potential explanation for the calculated TM temperatures being 50°C higher than the measured values is that the gamma heating rates were approximately 13% lower than the calculated values. The calculations were performed for VXF-15 in the HFIR reflector. When it was time to insert the experiment, VXF-15 was already occupied, so the experiment was irradiated in VXF-9. Scoping calculations indicate that gamma heating rates in VXF-9 are ~2% lower than those in VXF-15, which would result in temperatures being ~8°C lower than the calculated values. After adjusting for all the identified discrepancies between the modeled vs. as-irradiated conditions, the calculated TM temperatures are still 33°C (~8%) higher than the measured values. It is certainly possible that the calculated heating rates could have an error in the range of 8%, considering the complexity of these calculations. The nuclear heating calculations require MCNP and ORIGEN calculations to simulate radiation transport from the core center to the reflector positions and calculate reaction rates in each cell. Furthermore, the calculations determine more than just prompt neutron and gamma heating. They also consider local decay heat and gamma heating originating from fission products that accumulate in the HFIR fuel and from component activation.

4.2 Fission Gas Release

The irradiation conditions in this test are distinctly different than historic nitride fuel irradiations that have measured fission gas release [12, 25]. The observed fission gas release was less than expected for some capsules. At the irradiation temperatures in this experiment, only athermal fission gas release from recoil is expected based on historic expectations [26]. However, the observed release is also below what is expected for recoil.

A plot of the fission gas recoil release vs. theory [36] for three cases with no wall absorption of recoils, half wall coverage with capture of recoils, and the kernel treated as dust with all recoils released is shown in Figure 13. The measured releases do not fit the expected pattern. The only way that this mismatch can be explained is: (1) if 3 of the 5 puncture tests had virtually 100% trap leakage (note that Capsule 226 is not included because it is composed of TRISO particles, which are not expected to release fission gases) or (2) if the fuel dishes absorbed a significant portion of the recoils (Kr-85 gas). A somewhat higher than expected gas release could be explained by cracks or fissures in the kernel, but much lower release is more difficult to explain unless the kernels have a non-fissile surface layer of some kind.

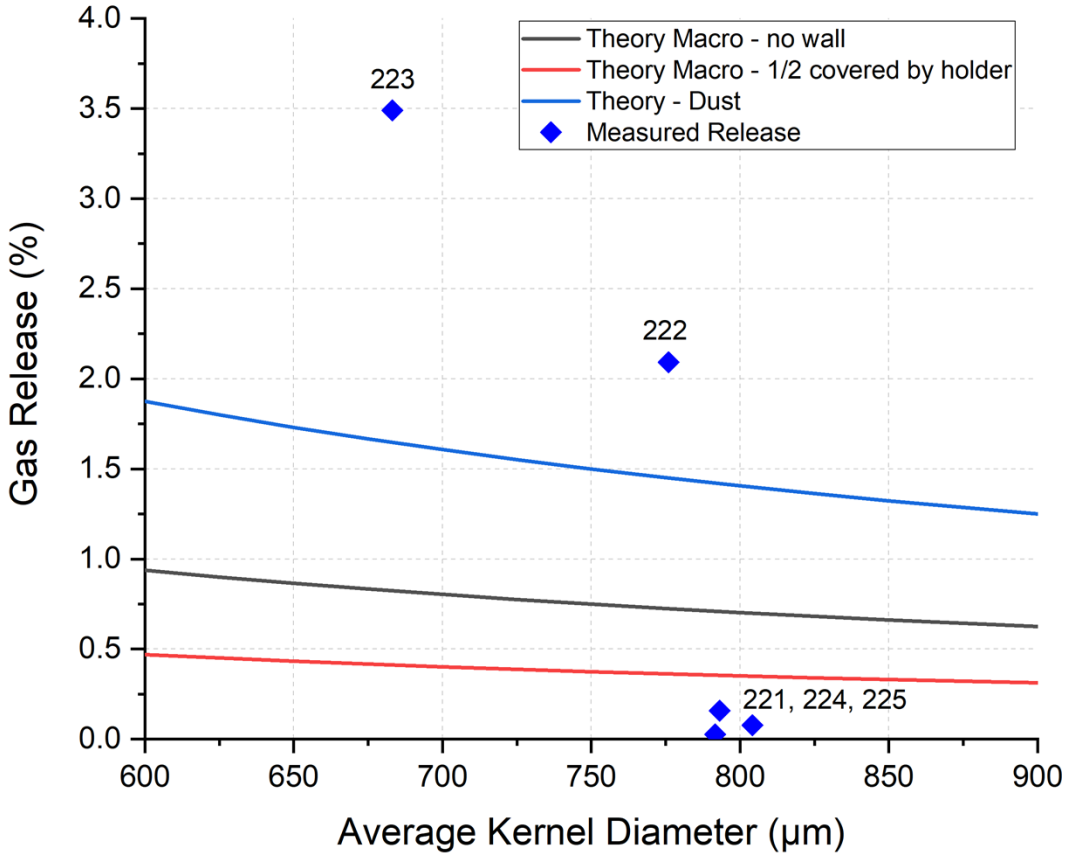

Figure 13. Measured Kr-85 gas release vs. average kernel diameter for each capsule compared with recoil theory. Data from Capsules 221, 224, and 225 with average kernel diameters near 800 µm do not conform to the theory.

After thoroughly inspecting the traps and procedures used in the fission gas release measurements, it was determined that no systematic loss of Kr-85 due to faulty equipment was impacting the reported fission gas release values. Thus, the results of the puncture testing are ambiguous. It is clear that the capsules remained sealed during irradiation, as evidenced by the fact that all capsules showed significant pressurization during puncture and that at least some of the kernels released 2–3% of their Kr-85. Further

PIE performed to date has not provided additional information on capsule irregularities that might have trapped fission gas during measurement. The next section discusses an oxygen rich outer layer that is present on the bare kernels, which may have had some effect on fission gas release. However, this layer would need to be mostly non-fissile material to reduce the recoils to such low levels, which is not the case.

4.3 Microstructure Examination

With optical microscopy, it is often possible to observe microstructural changes in the fuel from irradiation that can lead to macroscopic changes in fuel behavior. While early irradiation-assisted sintering may result in densification, swelling in particular should begin to increase porosity or impact porosity in the fuel and could possibly change the shape of the pores. In addition to optical microscopy, SEM and energy-dispersive x-ray spectroscopy (EDS) was used to identify the approximate composition of any secondary phases observed in the optical microscopy. For this low irradiation, few observations can be made concerning microstructural changes in the fuel. The porosity and morphology of the kernel pores do not differ in a noticeable way from the as-fabricated microstructure. It was possible to use backscatter electron (BSE) imaging of the samples to observe secondary phases and the grain structure of the irradiated kernels. This is shown in Figure 14 for a $U_{0.98}Gd_{0.02}C_{0.15}N_{0.85}$ kernel (MF01-224-02). From these images, the grain size was measured to be 31 ± 6 μm, which is not significantly different from the as-fabricated grain size.

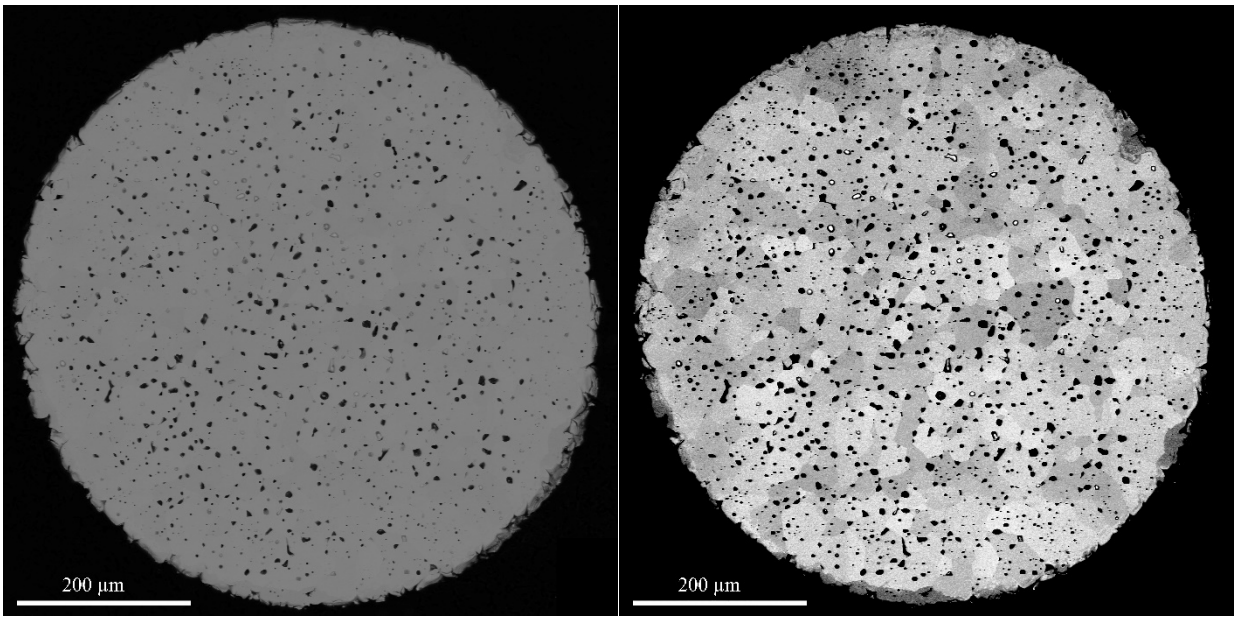

(a) (b)

Figure 14. (a) BSE image of a $U_{0.98}Gd_{0.02}C_{0.15}N_{0.85}$ kernel (MF01-224-02) at low contrast to reveal secondary phases and (b) high contrast to reveal grain structure.

There are secondary phases present on the periphery of the bare kernels in Figure 7 through Figure 11. These peripheral secondary phases observed in the optical microscopy were confirmed to be oxygen rich phases in the SEM. The oxygen rich phases observed on the periphery of the kernels are an artifact from fabrication where kernels were removed from the conversion furnace and stored in air prior to the coating layer deposition via fluidized bed chemical vapor deposition to produce UN TRISO. The oxygen rich phases are illustrated in Figure 15 using optical microscopy, BSE imaging, and EDS mapping of oxygen. The oxygen rich phases are also indicated by the white arrows in Figure 15a. In this area, there are oxygen-rich areas on the boundary between the kernel and the epoxy, and they are also located in a pore that was open to the free surface of the kernel. Closed porosity in the kernels do not exhibit the

oxygen rich phase on their perimeters. No fission product rich phases were observed. At this burnup, it appears that solid fission products are either miscible in the fuel matrix or distributed in such fine precipitates that they are invisible via SEM / EDS techniques. Follow on research will elucidate this area by applying transmission electron microscopy to these fuels.

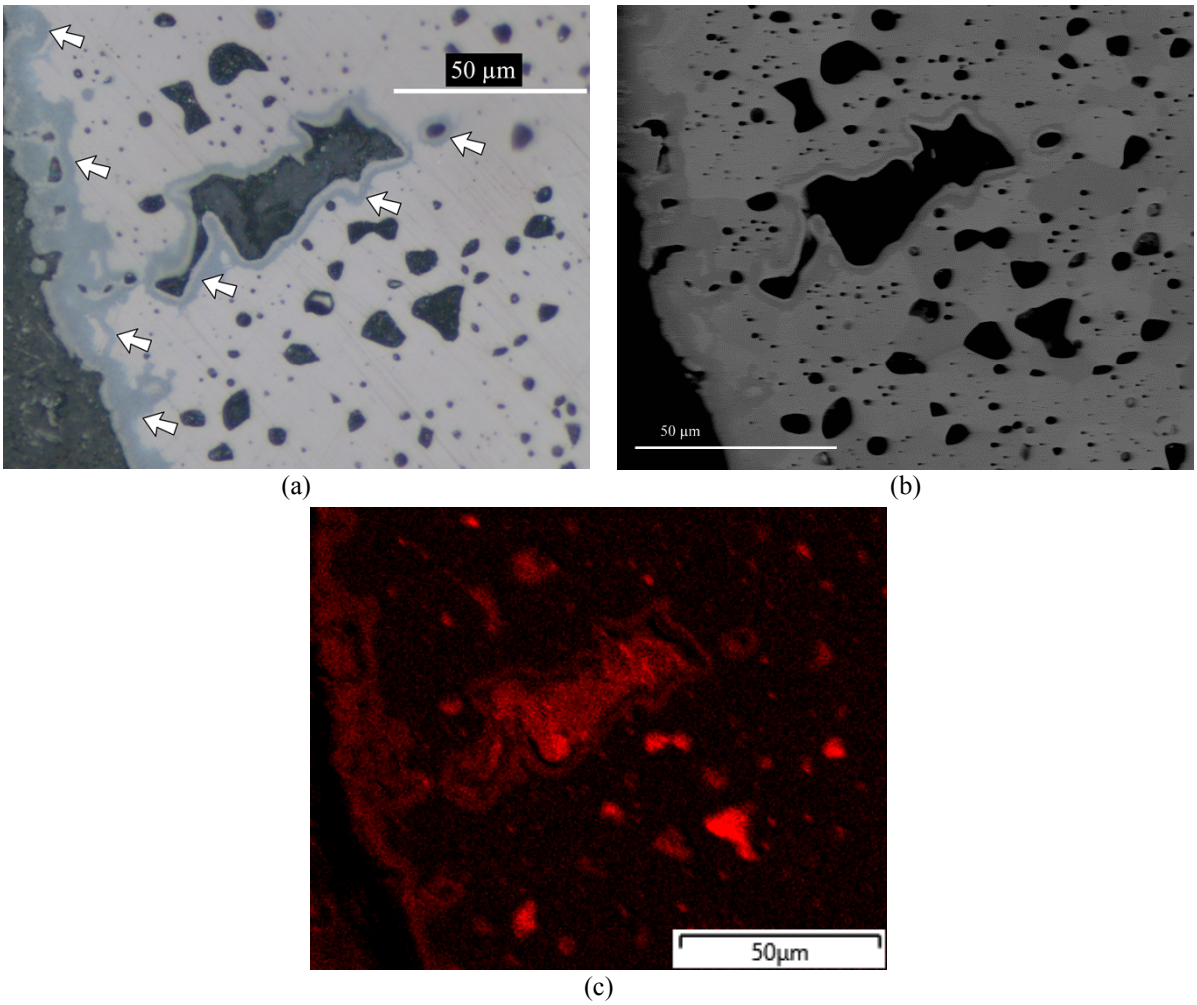

(a) (b)

(c)

Figure 15. Secondary oxygen rich phases observed on the periphery of a $UC_{0.11}N_{0.89}$ kernel (MF01-225-06) imaged by (a) optical microscopy with white arrows pointing towards the oxygen rich phase, (b) BSE imaging, and (c) oxygen EDS mapping of the same area.

Analysis by EDS of the Gd bearing kernels showed that there was some Gd fully dissolved into the UN matrix. However, there were also secondary phases present in the Gd bearing kernels, as well, which were confirmed to be Gd-bearing by SEM/EDS analysis. These phases were quite small and well dispersed in both compositions, as shown in Figure 16. In the $U_{0.89}Gd_{0.11}C_{0.11}N_{0.89}$ kernels, the extra Gd also led to some Gd rich phases that were on the periphery of the kernel, as well. This same behavior was observed in the as-fabricated kernels and was likely a result of nonoptimized internal gelation and conversion parameters for this composition. The external secondary phases were a mixture of Gd phases and phases with Gd and O. These phases are shown in BSE in Figure 17 and by EDS mapping in Figure 18. The mixed EDS map in Figure 18 shows the major UN phase in purple, the Gd secondary phases in green, an oxidized U phase in orange, and an oxidized Gd phase in yellow. A sulfur signal was also consistently observed in the Gd phases. EDS analysis showed approximately 0.6 atoms of S per atom of Gd in these precipitates. This S was likely carried over from fabrication during which Tamol SN, a

synthetic naphthalene sulfonate dispersant, was used [23]. Sulfur was only observed in Gd phases internal to the kernel and was not observed in Gd phases on the periphery of the kernel. Mass spectrometry analysis of the Gd bearing kernels also confirmed the elemental concentration of Gd in these kernels and the isotopic distribution of the remaining Gd. The Gd isotopics were enriched in Gd-156 and Gd-158 and were depleted in Gd-155 and Gd-157 compared with natural Gd isotopics, as would be expected from irradiation in a neutron field. Notably, Gd is not transmuting to a different element. Any modifications in chemical or atomic fuel properties that result from Gd additions were not impacted by this level of neutron irradiation. In part because the majority of Gd transmutation resulted in more Gd, SEM/EDS analysis of the Gd bearing kernels at this burnup revealed little if any change in microstructure at this level of irradiation even though the as-irradiated neutronic properties (Gd isotopics) of this fuel were quite different from the original as-fabricated composition.

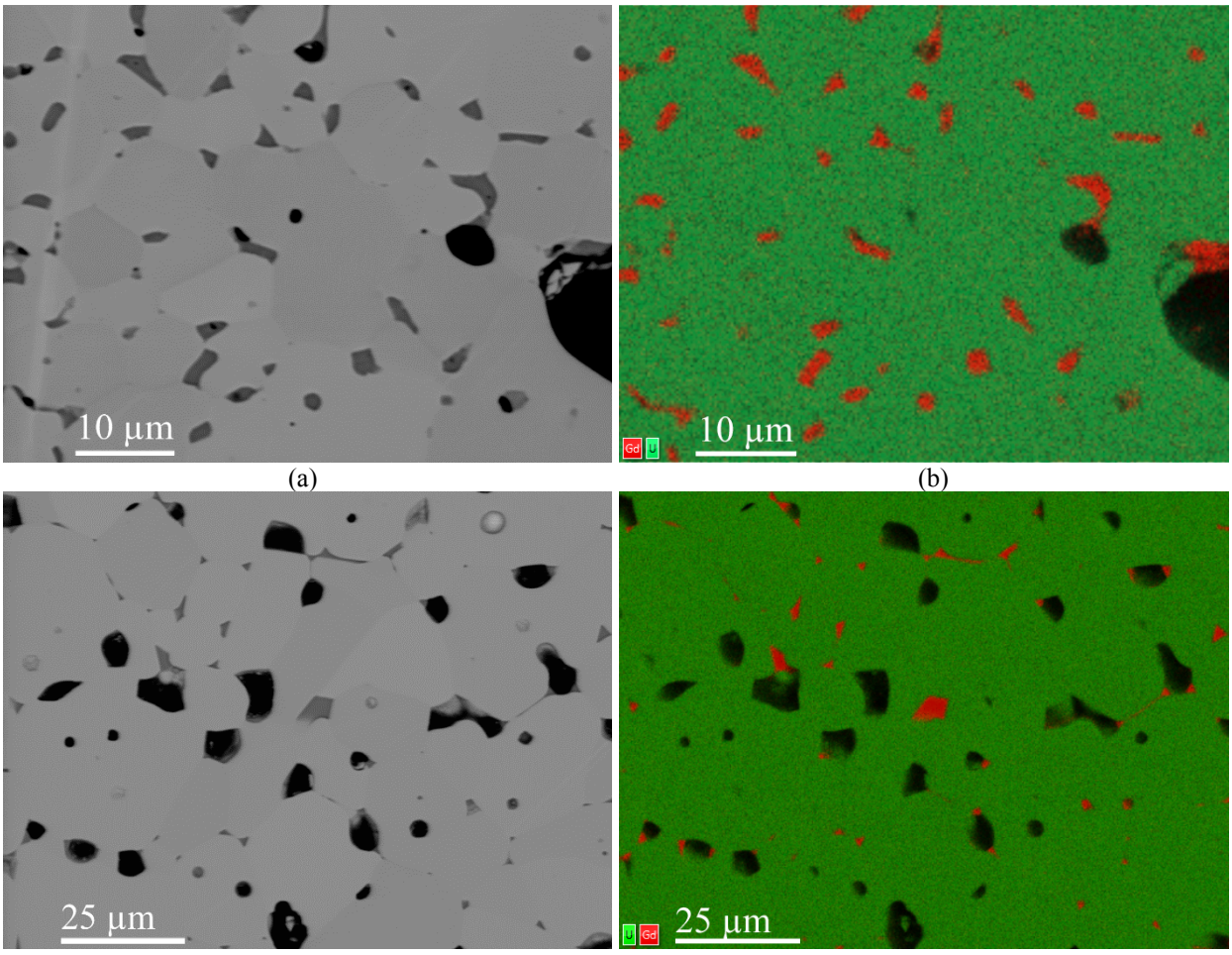

(a) (b)

(c) (d)

Figure 16. (a) BSE image of the general microstructure of a $U_{0.89}Gd_{0.11}C_{0.11}N_{0.89}$ kernel (MF01-223-04) showing Gd bearing secondary phases in dark gray. (b) An EDS map of the same area showing U content in green and Gd content in red. (c) BSE image of the general microstructure of a $U_{0.98}Gd_{0.02}C_{0.15}N_{0.85}$ kernel (MF01-224-02) showing Gd bearing secondary phases in dark gray. (d) An EDS map of the same area as (c) showing U content in green and Gd content in red.

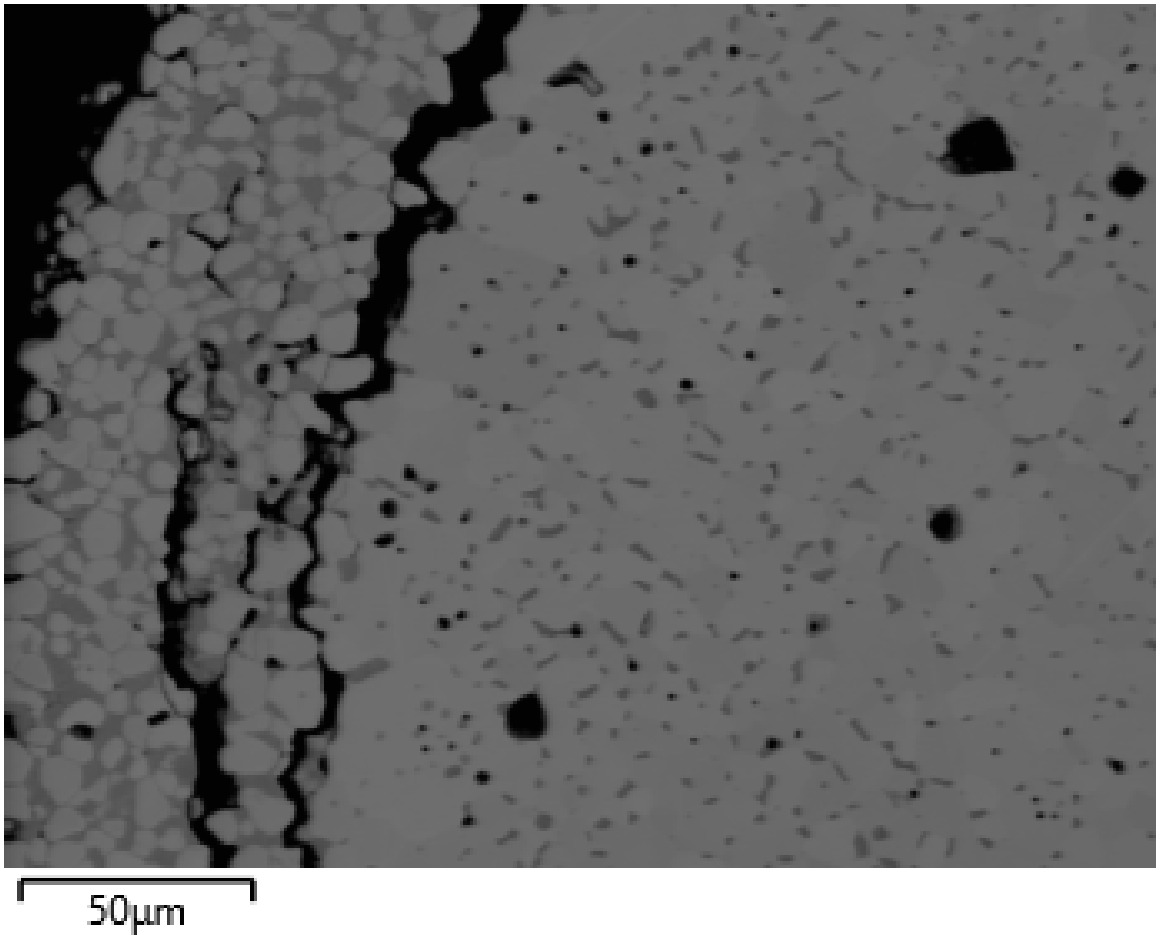

Figure 17. BSE image of the edge of an irradiated $U_{0.89}Gd_{0.11}C_{0.11}N_{0.89}$ particle, MF01 223-04, showing the oxidized Gd and U on the edge and Gd secondary phases in the interior.

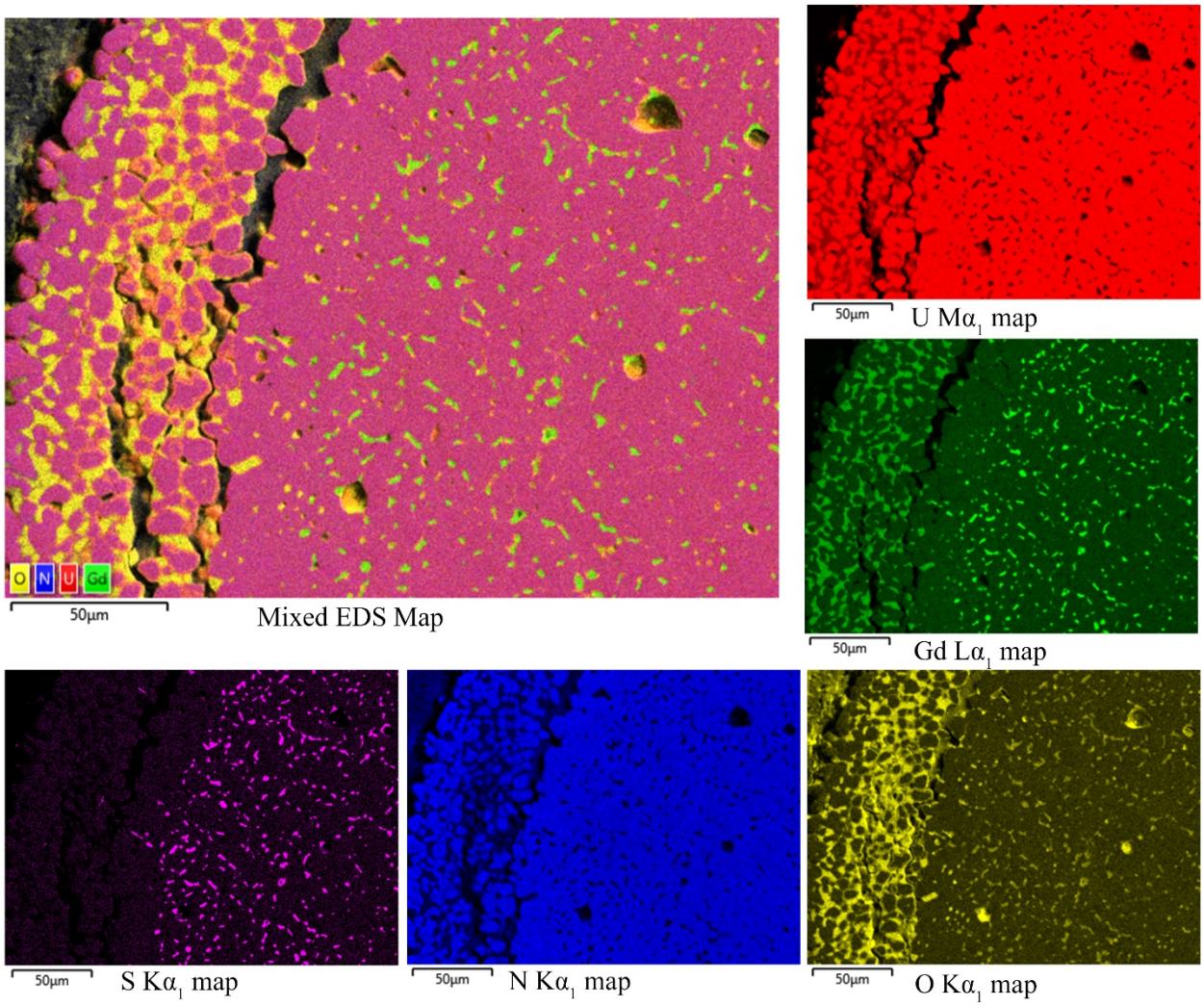

Figure 18. The top left image shows the EDS mapping of the area shown in Figure 17, highlighting the different observed phases, including UN (purple), oxidized U (orange), Gd secondary phases (green), and oxidized Gd phases (yellow). The individual EDS maps of these elements are also shown. Additionally, an individual EDS map for S is presented, which demonstrates that S is limited to the internal Gd phases.

Figure 19 shows a BSE image of the interface between the UN kernel and the buffer layer in one of the irradiated UN TRISO particles (MF01 226-02). There is evidence of some interaction between the kernel and buffer, where a bright layer decorates the inner (~1 µm) edge of the buffer layer in Figure 19. The range of fission fragment recoil into the buffer is ~30 µm and, it does not explain this concentrated bright layer. It may be due to the deposition of volatile fission products on this surface or small chemical interaction between the kernel and buffer at the start of irradiation prior to buffer shrinkage and debonding. This is often observed in uranium oxide / uranium carbide kernel TRISO particles [37–41]. A slight gap (~10 µm) opened between the kernel and the buffer, which is also typical and is due to buffer shrinkage due to densification as a result of irradiation induced displacements. As with the rest of the kernels, no fission product phases were observed in the kernel, and no fission product precipitates were observed at the inner pyrolytic carbon layer-SiC layer interface, as shown in Figure 20. A circumferential crack in the SiC layer formed during sample preparation, which is also evident in Figure 12. This crack is believed to be due to sample preparation, not irradiation-induced stresses. However, a similar crack did form during the preparation of both UN TRISO particles that were prepared. No evidence of a crack was

observed in the XCT of MF01 226-04, further supporting the suggestion that this crack was induced during sample preparation.

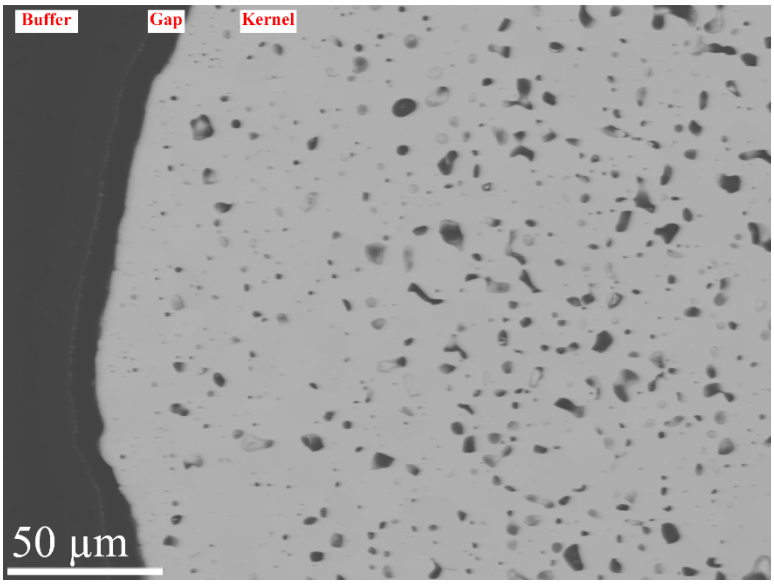

Figure 19. BSE image of the kernel/buffer interface in an irradiated UN TRISO particle (MF01 226-02).

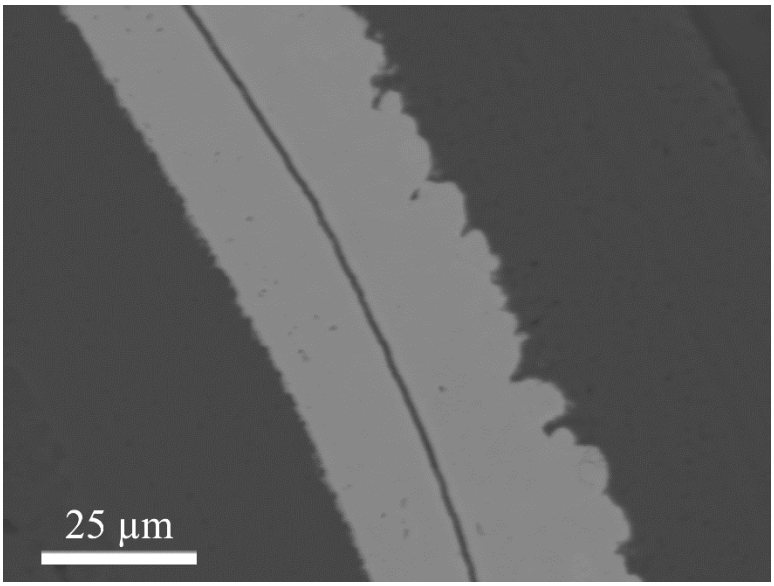

Figure 20. BSE image of the SiC layer of an irradiated UN TRISO particle and its interface with the inner and outer pyrolytic carbon layers.

5. SUMMARY

This work summarizes PIE from the first set of MiniFuel irradiation experiments that included variants of UN kernels and TRISO particles. Because the MiniFuel experiments are significantly different than traditional fueled experiments, this PIE served as a shakedown test of the PIE techniques that will be applied to future MiniFuel experiments. Experimental evaluations of burnup (i.e., isotopic analysis) and temperature (passive SiC TMs) have provided valuable feedback for simulations of MiniFuel targets that are currently being designed and fabricated for insertion into HFIR. Additionally, several types of

examinations were conducted to evaluate fission gas release, visual appearance, gamma-emitting fission product content, chemical content, and microstructure of the UN fuel specimens. Overall, the irradiated UN kernels and UN TRISO particles are still intact and do not show any consequence of irradiation at this low burnup. The results from fission gas release measurements are mixed. As expected, no fission gas release was seen in the capsule that contained the UN TRISO particles. Some release that is generally in line with recoil release was observed in Capsules 222 and 223. Further investigation of the fission gas release observed for Capsules 221, 224, and 225 is still needed to understand the low Kr-85 activity observed for these capsules. The capsule disassembly showed that it was possible to remove the particles from the Mo cups and to retain pre-irradiation particle identities. However, this process can still be improved, considering that some particle identification was lost during disassembly. The microstructural examination of these kernels revealed good performance for these irradiation conditions. Very few irradiation-induced changes can be observed in the microstructure. These positive results justify the continuation of ongoing irradiations of UN kernels and UN TRISO to higher burnups (~6% FIMA) and more generally show how the MiniFuel design can be used for the rapid screening of novel fuel concepts.

Acknowledgments

Several ORNL staff members contributed to the collection of the data discussed in this work. Mass spectrometry on the fuel was performed by Tamara Keever and Benjamin Roach. The hot-cell staff at the Irradiated Fuel Examination Laboratory, including Zachary Burns, Tyson Jordan, Darren Skitt and Chuck Baldwin, were instrumental in data collection. Special recognition for the support of this experiment also goes to Annabelle Le Coq, Kory Linton, Grant Helmreich and Alicia Raftery. Andrew Nelson and Tyler Gerczak provided valuable comments on the manuscript. The work was supported by the Advanced Fuels Campaign of the DOE Office of Nuclear Energy. A portion of this research used resources at HFIR, a DOE Office of Science User Facility operated by ORNL.

References

[1] D.C. Crawford, D.L. Porter, S.L. Hayes, M.K. Meyer, D.A. Petti, K. Pasamehmetoglu, An approach to fuel development and qualification, J. Nucl. Mater. 371 (2007) 232–242. doi:10.1016/J.JNUCMAT.2007.05.029.

[2] K.A. Terrani, N.A. Capps, M.J. Kerr, C.A. Back, A.T. Nelson, B.D. Wirth, S.L. Hayes, C.R. Stanek, Accelerating Nuclear Fuel Development and Qualification: Engineering-Scale Modeling and Simulation Integrated with Separate Effects Testing, J. Nucl. Mater. 539 (2020) 152267. doi:10.1016/j.jnucmat.2020.152267.

[3] C.M. Petrie, J.R. Burns, A.M. Raftery, A.T. Nelson, K.A. Terrani, Separate effects irradiation testing of miniature fuel specimens, J. Nucl. Mater. 526 (2019) 151783. doi:10.1016/j.jnucmat.2019.151783.

[4] K.G. Field, J.L. McDuffee, J.W. Geringer, C.M. Petrie, Y. Katoh, Evaluation of the continuous dilatometer method of silicon carbide thermometry for passive irradiation temperature determination, Nucl. Instruments Methods Phys. Res. Sect. B Beam Interact. with Mater. Atoms. 445 (2019) 46–56. doi:https://doi.org/10.1016/j.nimb.2019.02.022.

[5] K.A. Terrani, B.C. Jolly, J.M. Harp, Uranium nitride tristructural-isotropic fuel particle, J. Nucl. Mater. 531 (2020) 152034. doi:10.1016/J.JNUCMAT.2020.152034.

[6] D.A. Petti, B.P. Collin, D. Marshall, A summary of the results from the DOE advanced gas reactor (AGR) fuel development and qualification program, Idaho Natl. Lab. Rep. (2017) INL/EXT-16-40784. doi:10.2172/1369357.

[7] P.A. Demkowicz, J.D. Hunn, S.A. Ploger, R.N. Morris, C.A. Baldwin, J.M. Harp, P.L. Winston, T.J. Gerczak, I.J. van Rooyen, F.C. Montgomery, C.M. Silva, Irradiation performance of AGR-1 high temperature reactor fuel, Nucl. Eng. Des. 306 (2016) 2–13. doi:10.1016/J.NUCENGDES.2015.09.011.

[8] J.D. Hunn, C.A. Baldwin, F.C. Montgomery, T.J. Gerczak, R.N. Morris, G.W. Helmreich, P.A. Demkowicz, J.M. Harp, J.D. Stempien, Initial examination of fuel compacts and TRISO particles from the US AGR-2 irradiation test, Nucl. Eng. Des. 329 (2018) 89–101. doi:10.1016/j.nucengdes.2017.09.017.
[9] C.A. Baldwin, J.D. Hunn, R.N. Morris, F.C. Montgomery, C.M. Silva, P.A. Demkowicz, First elevated-temperature performance testing of coated particle fuel compacts from the AGR-1 irradiation experiment, Nucl. Eng. Des. 271 (2014) 131–141. doi:10.1016/j.nucengdes.2013.11.021.
[10] R.N. Morris, J.D. Hunn, C.A. Baldwin, F.C. Montgomery, T.J. Gerczak, P.A. Demkowicz, Initial results from safety testing of US AGR-2 irradiation test fuel, Nucl. Eng. Des. 329 (2018) 124–133. doi:10.1016/j.nucengdes.2017.08.006.
[11] R.N. Morris, C.A. Baldwin, P.A. Demkowicz, J.D. Hunn, E.L. Reber, Performance of AGR-1 high-temperature reactor fuel during post-irradiation heating tests, Nucl. Eng. Des. 306 (2016) 24–35. doi:10.1016/J.NUCENGDES.2016.04.031.
[12] Y. Arai, Nitride Fuel, Compr. Nucl. Mater. (2012) 41–54. doi:10.1016/B978-0-08-056033-5.00050-1.
[13] J.B.T.-R.M. in M.S. and M.E. Wallenius, Nitride Fuels☆, in: Elsevier, 2019. doi:https://doi.org/10.1016/B978-0-12-803581-8.11694-7.
[14] B. Hilton, D. Porter, S. Hayes, AFC-1 Transmutation Fuels Post-Irradiation Hot Cell Examination 4-8 at.% - Final Report (Irradiation Experiments AFC-1B, -1F and -1Æ), Idaho Natl. Lab. Rep. (2006) INL/EXT-05-00785. doi:10.2172/911779.
[15] J.M. Harp, S.L. Hayes, P.G. Medvedev, D.L. Porter, L. Capriotti, Testing Fast Reactor Fuels in a Thermal Reactor: A Comparison Report, Idaho Natl. Lab. Rep. (2017) INL/EXT-17-41677. doi:10.2172/1458766.
[16] T.M. Besmann, M.K. Ferber, H.-T. Lin, B.P. Collin, Fission product release and survivability of UN-kernel LWR TRISO fuel, J. Nucl. Mater. 448 (2014) 412–419. doi:10.1016/j.jnucmat.2013.10.034.
[17] H. Matzke, Science of advanced LMFBR fuels, Elsevier Science Pub. Co. Inc.,New York, NY, United States, 1986. https://www.osti.gov/biblio/6332409.
[18] N. George, G.I. Maldonado, K.A. Terrani, A. Godfrey, J.C. Gehin, Preliminary evaluation of burnable poisons in uranium-based fully ceramic microencapsulated fuel for PWRs, in: Trans. Am. Nucl. Soc., 2012.
[19] J.W. McMurray, R.D. Hunt, C.M. Silva, G.W. Helmreich, R.L. Seibert, Production of UN kernels with Gd additive as burnable absorber, Oak Ridge Natl. Lab. Rep. (2018) ORNL/SPR-2018/27 rev. 1.
[20] C.M. Petrie, J.R. Burns, R.N. Morris, K.R. Smith, A.G. Le Coq, K.A. Terrani, Irradiation of Miniature Fuel Specimens in the High Flux Isotope Reactor, Oak Ridge Natl. Lab. Rep. (2018) ORNL/SR-2018/874. doi:10.2172/1458354.
[21] J.W. McMurray, Fuel Material Certification Document Memo McMurray to Petrie, (2018).
[22] B. Jolly, G. Helmreich, J. Dyer, K.A. Terrani, FABRICATION AND CHARACTERIZATION OF DU and LEU UN TRISO PARTICLES, Oak Ridge Natl. Lab. Rep. (2016) ORNL/LTR-2016/384.
[23] J.W. McMurray, R.D. Hunt, T.J. Reif, G.W. Helmreich, C.M. Silva, R.L. Seibert, T.J. Gerczak, K.A. Terrani, Investigation of sol-gel feedstock additions and process variables on the density and microstructure of UN microspheres, J. Nucl. Mater. 520 (2019) 78–86. doi:10.1016/j.jnucmat.2019.04.003.
[24] R.W. Stratton, G. Ledergerber, F. Ingold, T.W. Latimer, K.M. Chidester, Fuel fabrication processes, design and experimental conditions for the joint US-Swiss mixed carbide test in FFTF (AC-3 test), J. Nucl. Mater. 204 (1993) 39–49. doi:https://doi.org/10.1016/0022-3115(93)90197-7.
[25] S.B. Ross, M.S. El-Genk, R.B. Matthews, Uranium nitride fuel swelling correlation, J. Nucl. Mater. 170 (1990) 169–177. doi:https://doi.org/10.1016/0022-3115(90)90409-G.
[26] K. Tanaka, K. Maeda, K. Katsuyama, M. Inoue, T. Iwai, Y. Arai, Fission gas release and swelling

in uranium–plutonium mixed nitride fuels, J. Nucl. Mater. 327 (2004) 77–87. doi:https://doi.org/10.1016/j.jnucmat.2004.01.002.
[27] R.B. Matthews, Irradiation performance of nitride fuels, in: United States, 1993. https://www.osti.gov/biblio/7368772.
[28] A.M. Raftery, R.N. Morris, K.R. Smith, G.W. Helmreich, C.M. Petrie, K.A. Terrani, A.T. Nelson, Development of a characterization methodology for post-irradiation examination of miniature fuel specimens, Oak Ridge Natl. Lab. Rep. (2018) ORNL/SPR-2018/918. doi:10.2172/1474563.
[29] J.M. Harp, P.A. Demkowicz, P.L. Winston, J.W. Sterbentz, An analysis of nuclear fuel burnup in the AGR-1 TRISO fuel experiment using gamma spectrometry, mass spectrometry, and computational simulation techniques, Nucl. Eng. Des. 278 (2014) 395–405. doi:10.1016/J.NUCENGDES.2014.07.041.
[30] B.D. Roach, C.R. Hexel, J.M. Guaquinto, Demonstration of a Rapid HPLC-ICPMS Direct Coupling Technique Using IDMS-Project Report: Part I, Oak Ridge, TN (United States), 2017. doi:10.2172/1456810.
[31] B.D. Roach, D.C. Glasgow, E.K. Fenske, R.H. Ilgner, C.R. Hexel, J.M. Giaquinto, Demonstration of a Rapid HPLC-ICPMS Direct Coupling Technique Using IDMS- Project Report: Part II, Oak Ridge, TN (United States), 2017. doi:10.2172/1435281.
[32] B.D. Roach, E.K. Fenske, R.H. Ilgner, C.R. Hexel, T.J. Haverlock, J.M. Giaquinto, Development of a fast and efficient analytical technique for the isotopic analysis of fission and actinide elements in environmental matrices, J. Chromatogr. A. 1587 (2019) 155–165. doi:10.1016/j.chroma.2018.12.029.
[33] B.D. Roach, J.M. Giaquinto, C.R. Hexel, R.H. Ilgner, E.K. Fenske, Method Development of a Rapid Analytical Technique for Nuclear Materials in Complex Matrices Using Isotope Dilution-High Pressure Ion Chromatography-Inductively Coupled Plasma Mass Spectrometry (ID-HPIC-ICPMS), in: INMM 58th Annu. Meet., Indian Wells, CA, USA, 2017. https://www.osti.gov/biblio/1468276.
[34] F.C. Montgomery, J.D. Hunn, T.J. Keever, B.D. Roach, R.H. Ilgner, E.K. Fenske, J.M. Giaquinto, Measurement of Average Burnup in TRISO-Coated Particles from AGR-2 UCO Compacts 2-2-2 and 6-4-2, Oak Ridge Natl. Lab. Rep. (2018) ORNL/TM-2018/931. doi:10.2172/1476419.
[35] W.J. Maeck, R.P. Larsen, J.E. Rein, Burnup Determination for Fast Reactor Fuels: A Review and Status of the Nuclear Data and Analytical Chemistry Methodology Requirements, U.S. At. Energy Comm. TID-26209 (1973).
[36] B.J. Lewis, Fission product release from nuclear fuel by recoil and knockout, J. Nucl. Mater. 148 (1987) 28–42. doi:https://doi.org/10.1016/0022-3115(87)90515-0.
[37] P.A. Demkowicz, J.D. Hunn, R.N. Morris, I.J. van Rooyen, T.J. Gerczak, J.M. Harp, S.A. Ploger, AGR-1 Post Irradiation Examination Final Report, Idaho Natl. Lab. Rep. (2015) INL/EXT-15-36407. doi:10.2172/1236801.
[38] I.J. Van Rooyen, T.M. Lillo, H. Wen, K.E. Wright, J.W. Madden, J.A. Aguiar, Advanced Electron Microscopy and Micro analytical technique development and application for Irradiated TRISO Coated Particles from the AGR-1 Experiment, Idaho Natl. Lab. Rep. (2017) INL/EXT-15-36281. doi:10.2172/1364087.
[39] J.D. Hunn, R.N. Morris, C.A. Baldwin, F.C. Montgomery, G.W.C. Silva, AGR-1 Irradiated Compact 6-1-1 PIE Report: Evaluation of As-Irradiated Fuel Performance Using Leach Burn Leach, IMGA, Materialography, and X-ray Tomography, Oak Ridge Natl. Lab. Rep. (2012) ORNL/TM-2012/233 rev.0.
[40] J.D. Hunn, R.N. Morris, C.A. Baldwin, F.C. Montgomery, G.W.C. Silva, AGR-1 Irradiated Compact 4-4-2 PIE Report : Evaluation of As-Irradiated Fuel Performance with Leach Burn Leach , IMGA , Materialography , and X-ray Tomography, Oak Ridge Natl. Lab. Rep. (2013) ORNL/TM-2013/236.
[41] J.D. Hunn, T.J. Gerczak, F.C. Montgomery, D.J. Skitt, C.A. Baldwin, G.W. Helmreich, B.D. Eckhart, J.A. Dyer, AGR-2 As-Irradiated UCO Compact 5-4-2 PIE Report, Oak Ridge Natl. Lab.

Rep. (2018) ORNL/TM-2018/863. doi:10.2172/1454396.

Supplemental Data

Table S.1. Decay-corrected activity (μCi) of selected fission products from the MF01 MiniFuel target.

Particle	*Zr-95*	*Ru-106*	*Cs-134*	*Cs-137*	*Ce-144*	*Eu-154*
221-01	5.73E + 03	9.83E + 02	2.63E + 01	6.68E + 01	1.50E + 03	1.77E + 00
221-02	6.01E + 03	1.03E + 03	2.79E + 01	6.98E + 01	1.56E + 03	1.77E + 00
221-03	6.05E + 03	1.01E + 03	2.80E + 01	7.03E + 01	1.59E + 03	1.72E + 00
221-04	4.72E + 03	8.22E + 02	2.15E + 01	5.62E + 01	1.25E + 03	1.40E + 00
221-05	5.32E + 03	9.16E + 02	2.43E + 01	6.27E + 01	1.41E + 03	1.54E + 00
221-06	4.98E + 03	8.60E + 02	2.31E + 01	5.91E + 01	1.31E + 03	1.56E + 00
222-01	8.33E + 03	9.85E + 02	4.31E + 01	9.80E + 01	2.35E + 03	2.40E + 00
222-02	6.46E + 03	7.74E + 02	3.37E + 01	7.70E + 01	1.81E + 03	1.81E + 00
222-03	8.26E + 03	9.79E + 02	4.27E + 01	9.69E + 01	2.33E + 03	2.36E + 00
222-04	8.57E + 03	1.02E + 03	4.46E + 01	1.01E + 02	2.42E + 03	2.79E + 00
222-05	7.87E + 03	9.42E + 02	4.08E + 01	9.29E + 01	2.22E + 03	2.39E + 00
222-06	6.49E + 03	7.83E + 02	3.45E + 01	7.90E + 01	1.82E + 03	1.87E + 00
223-01	3.82E + 03	4.56E + 02	1.94E + 01	4.32E + 01	1.05E + 03	1.07E + 00
223-02	5.36E + 03	6.54E + 02	2.63E + 01	6.03E + 01	1.46E + 03	1.44E + 00
223-03	5.62E + 03	7.00E + 02	2.85E + 01	6.33E + 01	1.55E + 03	1.51E + 00
223-04	5.32E + 03	6.58E + 02	2.63E + 01	5.94E + 01	1.48E + 03	1.43E + 00
223-05	4.65E + 03	5.73E + 02	2.27E + 01	5.23E + 01	1.29E + 03	1.25E + 00
223-06	3.26E + 03	3.99E + 02	1.69E + 01	3.83E + 01	8.94E + 02	9.40E-01
224-01	8.03E + 03	9.75E + 02	4.23E + 01	9.18E + 01	2.24E + 03	2.39E + 00
224-02	8.01E + 03	9.58E + 02	4.13E + 01	9.10E + 01	2.25E + 03	2.22E + 00
224-03	7.72E + 03	9.35E + 02	4.04E + 01	8.81E + 01	2.18E + 03	2.27E + 00
224-04	8.09E + 03	9.56E + 02	4.14E + 01	9.14E + 01	2.25E + 03	2.23E + 00
224-05	8.14E + 03	9.78E + 02	4.24E + 01	9.25E + 01	2.26E + 03	2.21E + 00
224-06	8.50E + 03	9.98E + 02	4.35E + 01	9.75E + 01	2.37E + 03	2.29E + 00
225-01	5.62E + 03	9.61E + 02	2.60E + 01	6.55E + 01	1.47E + 03	1.63E + 00
225-02	5.05E + 03	8.70E + 02	2.28E + 01	5.90E + 01	1.33E + 03	1.56E + 00
225-03	5.75E + 03	9.66E + 02	2.68E + 01	6.67E + 01	1.51E + 03	1.69E + 00
225-04	6.27E + 03	1.08E + 03	2.88E + 01	7.37E + 01	1.63E + 03	1.96E + 00
225-05	5.31E + 03	8.84E + 02	2.45E + 01	6.17E + 01	1.40E + 03	1.53E + 00
225-06	5.12E + 03	8.87E + 02	2.37E + 01	5.99E + 01	1.34E + 03	1.53E + 00
226-01	6.07E + 03	1.01E + 03	2.77E + 01	7.11E + 01	1.59E + 03	1.78E + 00
226-02	5.65E + 03	9.82E + 02	2.58E + 01	6.65E + 01	1.47E + 03	1.57E + 00
226-03	5.54E + 03	9.59E + 02	2.57E + 01	6.62E + 01	1.45E + 03	1.71E + 00
226-04	5.05E + 03	8.73E + 02	2.27E + 01	5.86E + 01	1.31E + 03	1.44E + 00